Comparison of Humidified Hydrogen and Partly Pre-Reformed Natural Gas as Fuel for Solid Oxide Fuel Cells applying Computational Fluid Dynamics

Andersson, Martin; Nakajima, Hironori; Kitahara, Tatsumi; Shimizu, Akira; Koshiyama, Takahiro; Paradis, Hedvig; Yuan, Jinliang; Sundén, Bengt

Published in:
International Journal of Heat and Mass Transfer

DOI:
10.1016/j.ijheatmasstransfer.2014.06.033

2014

Comparison of Humidified Hydrogen and Partly Pre-Reformed Natural Gas as Fuel for Solid Oxide Fuel Cells applying Computational Fluid Dynamics

Martin Andersson, Hironori Nakajima, Tatsumi Kitahara, Akira Shimizu, Takahiro Koshiyama, Hedvig Paradis, Jinliang Yuan and Bengt Sundén.

Accepted for publication in Int J Heat and Mass Transport

DOI: 10.1016/j.ijheatmasstransfer.2014.06.033

Abstract

A three-dimensional computational fluid dynamics (CFD) approach based on the finite element method (FEM) is used to investigate a solid oxide fuel cell (SOFC). Governing equations for heat, gas-phase species, electron, ion and momentum transport are implemented and coupled to kinetics describing electrochemical as well as internal reforming reactions. The model cell design is based on a cell from Ningbo Institute of Material Technology and Engineering in China and the electrochemical area-to-volume ratios are based on experimental work performed at Kyushu University in Japan.

A parameter study is performed focusing on the inlet fuel composition, where humidified hydrogen, 30 % pre-reformed natural gas (as defined by IEA) and 50 % pre-reformed natural gas (as defined by Kyushu University) are compared. It is found that when 30 % pre-reformed natural gas is supplied as fuel the air mass flow rate is halved, compared to the case with humidified hydrogen, keeping the inlet and outlet temperatures constant. The current density is decreased but the fuel utilization is kept at 80 %. It is found that the cathode support layer has a significant oxygen gas-phase resistance in the direction normal to the cathode/electrolyte interface (at positions under the interconnect ribs), as well as an electron resistance inside the cathode (at positions under the air channel) in the same direction. The

methane steam reforming reaction is shown, both according to the experiments and to the models, to proceed along the main flow direction throughout the cell.

Keywords: SOFC, 3D, FEM, modeling, cell scale, internal reforming, methane steam reforming reaction, water-gas shift reaction.

Highlights

- FEM approach with heat, mass, momentum and charge transport equations
- Comparison between hydrogen and pre-reformed natural gas as fuel
- Gas-phase oxygen resistance at positions under the interconnect ribs
- Electron resistance at positions under the air channel

1 Introduction

Solid oxide fuel cells (SOFCs) offer the possibility of environmentally friendly production of electricity by high efficiency, low emissions of pollutants and several options of fuels [1-2]. Besides the advantages of planar intermediate temperature SOFCs with simplicity in manufacturing and high power density, they can also be combined with gas turbines for co-generative applications. An intermediate operating temperature is here defined to 1000-1100 K (723-823 °C). For lower operating temperatures other materials than standard YSZ and LSM have to be considered. However, the commercialization of SOFC still has some challenges to overcome. SOFC still suffers from high manufacturing costs [3]. To address this problem the operational temperature can be lowered which would open up for a broader variety of material choices [4].

Mathematical modeling of SOFCs is a useful tool to achieve a more successful device by investigating structural and operating parameters for further optimization. It should be noted that computational fluid dynamics (CFD) models make it possible to reduce the amount of experiments needed for cell development, and only a limited amount of tests is then required to validate the accuracy of the models. Modeling the physical transport processes in an SOFC is challenging because of the interactions of transport, chemistry and electrochemistry occurs at different time and length scales simultaneously. Understanding these interactions are critical for optimal performance and cell design [5-6].

The most commonly listed limiting factors for an SOFC operation are activation, ohmic, and concentration polarizations. To handle these polarizations, the heat and mass transfer can be improved to satisfy the uniform and sufficient distribution of reactants within the porous electrode [3]. Concentration polarization becomes increasingly important when SOFC operates at high current densities and high hydrogen utilization (> 70%). At high hydrogen utilization (as well as high current density) the need of the fresh reactants is high at the three-phase boundary (TPB) which demands efficient diffusion of gases through the porous media [7]. The transport processes taking place within an SOFC are sometimes difficult to measure by experiments at high operating temperatures in which case computational modeling can be useful. The aim of this paper is to compare different fuel mixtures for planar anode-supported SOFCs, in terms of open circuit voltage, ion and electron current density, different polarization as well as gas-phase molecular distributions. The method applied in this study is the Finite Element Method (FEM) and the model is built in three-dimensions. The unique features of our model includes the study of the electron and oxygen ion transport limitations in the direction normal to the cathode/electrolyte interface, which was not possible to study in our previous 2D models [23,25-26]. The electron limitation occur at positions in the cathode

under the air channel and the oxygen gas-phase limitation occur at positions in the cathode under the interconnect ribs. Further design optimization is possible based on the local distribution of the different polarizations, ions, electrons as well as gas-phase species. The model cell design is based on a cell from Ningbo Institute of Material Technology and Engineering (NIMTE) in China. The electrochemical area-to-volume ratios are based on experimental work performed at Kyushu University in Japan [8]. Also the selection of the methane steam reforming reaction (MSR) kinetics is based on results from experimental work, performed at Kyushu University.

SOFCs with a supportive anode structure are usually built up by nickel/yttria stabilized zirconia (Ni/YSZ) cermet with high electrochemical performance and good chemical stability (see Fig. 1). If hydrogen is used as fuel, the active species involved in the electrochemical reactions are oxygen and hydrogen, as shown in eqns (1)-(2). H_2 forms a molecule of H_2O during this oxidation reaction and releases electrons [9-10]. The electrochemical reactions occur at the TPBs, i.e., the region where the electronic (Ni or lanthanum strontium manganite (LSM)), ionic (YSZ) and gas phases meet each other. Conduction of electrons occurs in the electronic-phase (Ni or LSM), oxygen ions migrate in the YSZ material (from the cathodic TPB to the anodic TPB through the electrolyte layer), and transport of gas molecules takes place in the open voids within the electrodes. Note that the TPB needs to be connected to the rest of the domain, i.e., the Ni- or LSM-phase must be connected throughout the specific electrode and further to the current collector, the pores need to be connected through the surrounding pore network to the fuel/air stream and the YSZ-phase in the electrodes to the YSZ electrolyte for charge transfer reactions to proceed [11]. As a fuel containing carbon monoxide and/or methane is supplied, the reforming reactions take place inside the anode. Carbon monoxide can be oxidized in the electrochemical reaction (eqn (3)), but also reacts

with water in the water-gas shift reaction (eqn (5, WGSR)) [12]. Notice that the WGSR is in general much faster than the carbon monoxide electrode reaction [13]. Methane reacts with steam in eqn (4, MSR).

$$\frac{1}{2}O_2 + 2e^- \Leftrightarrow O^{2-} \quad (1)$$

$$H_2 + O^{2-} \Leftrightarrow H_2O + 2e^- \quad (2)$$

$$CO + O^{2-} \rightarrow CO_2 + 2e^- \quad (3)$$

$$CH_4 + H_2O \Leftrightarrow 3H_2 + CO \quad \text{(MSR, 4)}$$

$$CO + H_2O \Leftrightarrow H_2 + CO_2 \quad \text{(WGSR, 5)}$$

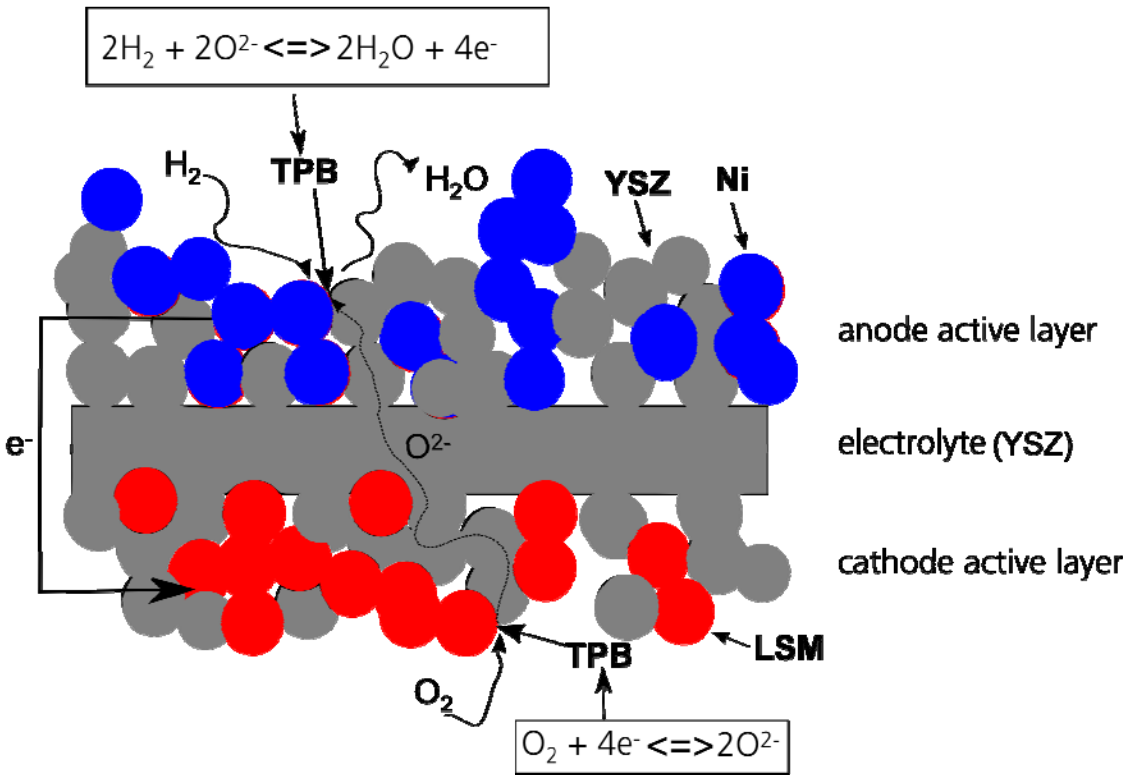

Figure 1. Schematic figure of the SOFC TPB structure.

2 FEM Model

A three dimensional model for a planar intermediate temperature SOFC is developed and

implemented in the commercial software COMSOL Multiphysics (version 4.3.1.161). However, the post processing is done with COMSOL Multiphysics version 4.4.0.150. Equations for heat, gas-phase species, ion, electron and momentum transport are solved simultaneously and coupled to kinetics describing the electrochemical reactions within the electrodes. The material structure parameters and geometry are selected based on a cell developed and tested at NIMTE, which is described in [14-15]. The geometry is defined in Table 1, and a sketch of the investigated cell can be seen in Fig. 2. Note that Fig. 2 is not to scale.

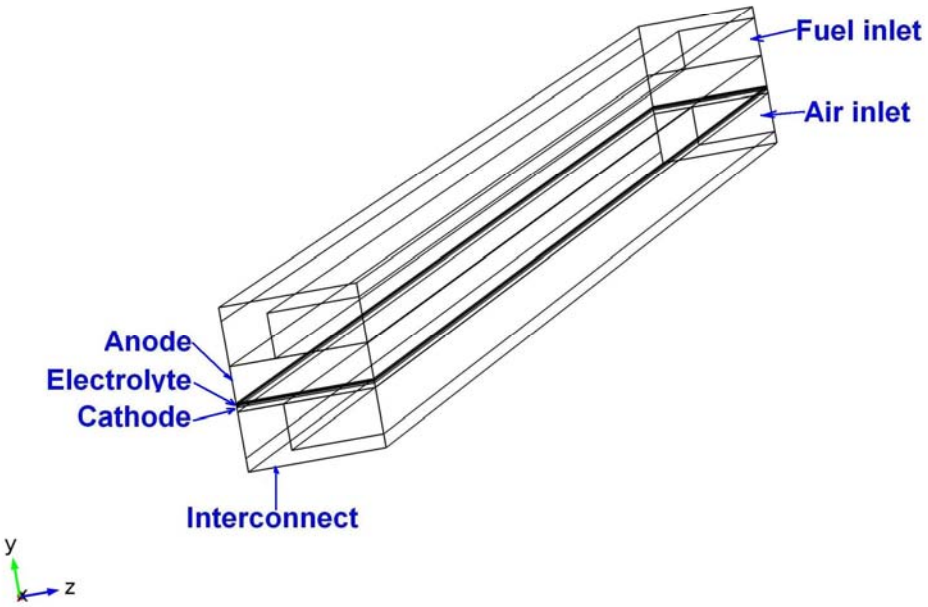

Figure 2. Schematic figure of the SOFC model.

Table 1: SOFC cell geometry

Cell Component	Direction	Thickness
Cell length	x	100 mm
Fuel & Air channel height	y	0.5 mm
Fuel & Air channel width	z	1 + 1 mm

Channel wall (rib) thickness	z	0.5 + 0.5 mm
Anode support layer thickness	y	400 μm
Anode active layer thickness	y	15 μm
Cathode support layer thickness	y	50 μm
Cathode active layer thickness	y	20 μm
Electrolyte thickness	y	10 μm
Interconnect thickness	y	150 +150 μm

2.1 Ion and Electron Transport as well as Electrochemical Reactions

Due to internal resistance and polarizations (overpotential losses) the actual voltage (E) becomes less than the open-circuit voltage. The actual voltage can be expressed as [16-17]:

$$E = E^{OCV} - \eta_{act} - \eta_{ohm} \tag{6}$$

Here, η are the respective polarizations. The polarizations other than η_{ohm} are defined as:

$$\eta_a = \phi_s - \phi_l - E_{eq,a} \tag{7}$$

$$\eta_c = \phi_s - \phi_l - E_{eq,c} \tag{8}$$

where ϕ is the potential, E_{eq} the equilibrium voltage. The index a stands for the anode, c for the cathode, s for the electrode material (Ni or LSM) and l for the electrolyte material (YSZ). For increased accuracy eqn (6) is not sufficient, instead the voltage can be expressed as the difference between the potentials at the anode and cathode current collectors [18]. However, eqn (6) is sufficient for the study performed in this work with focus on the heat and mass transport.

The electromotive force (reversible open-circuit voltage, E^{OCV}) in eqn (6) is determined by the difference in the thermodynamic potentials of the electrode reactions. When a hydrogen-

steam mixture is used as fuel, it can be calculated by the Nernst equation (eqn (9)) [19-20].

$$E_{H_2/O_2}^{OCV} = E_{H_2/O_2}^{0} - \frac{\mathrm{R}\cdot T}{2\cdot \mathrm{F}}\cdot \ln\left(\frac{p_{H_2O,TPB}}{p_{H_2,TPB}\sqrt{p_{O_2,TPB}}}\right) \tag{9}$$

$$E_{H_2/O_2}^{0} = 1.253 - 2.4516\cdot 10^{-4}\cdot T \tag{10}$$

where E^0 is the temperature dependent open-circuit voltage at standard pressure (1 atm) and p_i the partial pressure, at the TPB, in atm. It should be noted that eqns (9)-(10) are developed fuel mixtures containing humidified hydrogen [21] and it is recommended to replace this expression in future extensions of our model to include the impact from hydrocarbons.

The Butler-Volmer equations are frequently used to describe the activation polarization/current density relationship. The exchange current density is then used to calculate the activation polarization, which depends on the active catalytic material for the electrochemical reactions. The generalized Butler-Volmer equation is

$$i = AV\cdot i_0\cdot\left[\frac{p_{H_2O,TPB}}{p_{H_2O,b}}\exp\left\{\frac{-\alpha n_{e,a}.\mathrm{F}\eta_a}{\mathrm{R}\cdot T}\right\} - \frac{p_{H_2,TPB}}{p_{H_2,b}}\exp\left\{\frac{(1-\alpha)n_{e,a}.\mathrm{F}\eta_a}{\mathrm{R}\cdot T}\right\}\right] \tag{11}$$

Here, p is the partial pressure at the TPB or b (bulk fluid within the gas channels) and n_e is the number of electrons transferred per reaction. In high current region with sufficiently large η_a where

$$\exp\left(\frac{-\alpha n_{e,a}.\mathrm{F}\eta_a}{\mathrm{R}\cdot T}\right) << \exp\left\{\frac{(1-\alpha)n_{e,a}.\mathrm{F}\eta_a}{\mathrm{R}\cdot T}\right\} \tag{12}$$

Eq. (11) can be rewritten as

$$i = -AV\cdot i_0\cdot\left[\frac{p_{H_2,TPB}}{p_{H_2,b}}\exp\left\{\frac{(1-\alpha)n_{e,a}.\mathrm{F}\eta_a}{\mathrm{R}\cdot T}\right\}\right] \tag{13}$$

leading to

$$\ln i = \ln(-AV \cdot i_0) + \left[\ln\left\{ \frac{p_{H_2,TPB}}{p_{H_2,b}} \right\} + \left\{ \frac{(1-\alpha) n_{e,a}.\mathrm{F}\eta_a}{\mathrm{R} \cdot T} \right\} \right] \tag{14}$$

Eq. 15 accordingly gives the concentration polarization when the activation polarization (charge transfer) is not negligible [22].

$$\begin{aligned} \eta_a &= \frac{\mathrm{R} \cdot T}{(1-\alpha) n_{e,a}.\mathrm{F}} \ln\left(\frac{-i}{AV \cdot i_0} \right) + \frac{\mathrm{R} \cdot T}{(1-\alpha) n_{e,a}.\mathrm{F}} \ln\left(\frac{p_{H_2,b}}{p_{H_2,TPB}} \right) \\ &= \eta_{act,a} + \eta_{conc,a} \end{aligned} \tag{15}$$

Thus

$$\eta_{conc,a} = \frac{\mathrm{R} \cdot T}{(1-\alpha) n_{e,a}.\mathrm{F}} \ln\left\{ \frac{p_{H_2,b}}{p_{H_2,TPB}} \right\} \tag{16}$$

On the other hand, when $i_0 >> i$, the electrochemical reaction is diffusion rate-limiting.

In this case, assuming $i \ / \ i_0 = 0$,

$$0 = \frac{p_{H_2O,TPB}}{p_{H_2O,b}} \exp\left\{ \frac{-\alpha n_{e,a}.\mathrm{F}\eta_a}{\mathrm{R} \cdot T} \right\} - \frac{p_{H_2,TPB}}{p_{H_2,b}} \exp\left\{ \frac{(1-\alpha) n_{e,a}.\mathrm{F}\eta_a}{\mathrm{R} \cdot T} \right\} \tag{17}$$

The electrochemical equilibrium is established at the TPB owing to the fast charge transfer rates. So,

$$\eta_a = \eta_{conc,a} = \frac{\mathrm{R} \cdot T}{n_{e,a\cdot} \cdot \mathrm{F}} \ln\left(\frac{p_{H_2O,TPB} \cdot p_{H_2,b}}{p_{H_2,TPB} \cdot p_{H_2O,b}} \right) \tag{18}$$

specified as [23]. In a similar manner,

$$\eta_{conc,c} = \frac{\mathrm{R} \cdot T}{\alpha n_{e,c} \cdot \mathrm{F}} \ln\left(\frac{p_{O_2,b}}{p_{O_2,TPB}} \right) \tag{19}$$

when both activation and concentration polarizations cannot be neglected.

When the mass transfer rate-limiting, that is, the concentration polarization is dominant,

$$\eta_{conc,c} = \frac{\mathrm{R} \cdot T}{n_{e,c} \cdot \mathrm{F}} \ln\left(\frac{p_{O_2,b}}{p_{O_2,TPB}} \right) \tag{20}$$

Assuming singe-step rate limiting reaction for two electrodes, then the sum of the potential must equal the Nernst potential, i.e., the transfer coefficient is 0.5 [24].

$$i_0 = \frac{\mathrm{R} \cdot T}{n_e \cdot \mathrm{F}} \cdot k_e'' \cdot \exp\left(\frac{-E}{\mathrm{R} \cdot T} \right) \tag{21}$$

where F is the Faraday's constant, k_e'' the pre-exponential factor (which is $6.54 \cdot 10^{11}$ $\Omega^{-1}m^{-2}$ for the anode and $2.35 \cdot 10^{11}$ $\Omega^{-1}m^{-2}$ for the cathode [25]), i_0 the exchange current density, R the ideal gas constant, AV_e the electrochemical active area-to-volume ratio and $E_{a,e}$ the activation energy (137 kJ/mol for the cathode and 140 kJ/mol for the anode [16]). The potential difference between the anode and the cathode current collectors corresponds to the total cell operating voltage. The electrochemical active area to volume ratio is determined by fitting the current density to measurements performed at Kyushu University (with 50 % pre-reformed natural gas as fuel), i.e., the effects from hydrocarbon fuels are included. It should be mentioned that a constant operating voltage of 0.7 V is applied in the model and the comparison to experimental data is only performed at this voltage.

The governing equations for the ion and electron transport are implemented according to eqns (22)-(23).

$$i_l = \nabla \bullet \left(-\sigma_l \nabla \phi_l \right) \tag{22}$$

$$i_s = \nabla \bullet \left(-\sigma_s \nabla \phi_s \right) \tag{23}$$

where σ is the ion/electron conductivity and ϕ is the potential. The electronic conductivities in the anode ($\sigma_{s,a}$) and the cathode ($\sigma_{s,c}$), and ionic conductivity in the YSZ ($\sigma_{l,el}$) are calculated as described in [26]. The actual length that ions and electrons are transported in the electrodes increases because of the effects of the material compositions and their microscopic structures. This is accounted for by using the structure-dependent tortuosity factors and volume fractions/porosities [26].

2.2 Momentum transport

The gases flow in the fuel and air channels, and in the porous electrodes. Equation (24) is introduced and solved for the momentum transport (gas flow) in the porous materials as well as in the fuel and air channels, simultaneously [27-28], i.e., the interface conditions between the porous electrodes and the gas channels do not need to be defined.

$$\left(\frac{\mu}{\kappa}+\rho\cdot\nabla\bullet\vec{\mathrm{u}}\right)\cdot\vec{\mathrm{u}}-\nabla\left[-p+\frac{1}{\varepsilon}\left\{\Psi-\left(\frac{-2}{3}\cdot\mu\right)(\nabla\bullet\vec{\mathrm{u}})\right\}\right]=\mathbf{F} \qquad (24)$$

Here $\mathbf{F}$ is the volume force vector, p the pressure, κ the permeability of the porous medium ($1.76\cdot10^{-11}$ m^2 is applied for all porous material in our model), $\vec{\mathrm{u}}$ the velocity vector, Ψ the viscous stress tensor. The viscosity (μ) and density (ρ) for the participating gas mixtures are dependent on local temperature and mole fractions, as described in [25].

2.3 Mass transport

The mass transfer rate in the SOFC electrodes depends on the operating and structural parameters, such as temperature, fuel composition, porosity, particle size and tortuosity factors. To improve the cell performance, the polarizations need to be minimized.

Concentration polarization depends on the effectiveness of the heat and mass transfer. In this study special interest is put on the effects of the mass transfer in an SOFC. A concentration gradient in the porous electrodes is present under normal operating conditions due to the fuel and oxidant consumption at the reaction sites. The differences in concentration between different locations within the cell induce concentration losses. In order to minimize the concentration losses, the heat and mass transfer need to be understood in detail. Mauro *et al.* [3] found that concentration polarization increases as the H_2 concentration in the inlet mixture decreases. Mauro *et al.* [3] also found that higher fuel consumption increases the concentration polarization. In other words, if there is low reactant consumption, small reactant concentration gradients are produced across the electrode. Hussain *et al.* [29] found that a limited mass transfer resulted in lower reactant concentration at the reaction sites which corresponds to an increased concentration polarization. It was also found that the concentration polarization increased with increasing current density.

Regarding mass transfer, three distinct physical mechanisms are present in an SOFC: convection, molecular diffusion and Knudsen diffusion. The Knudsen diffusion is only relevant in the electrodes. Moreover, molecular diffusion in the cathode is usually binary (because the oxidant is oxygen from air (assumed to be made up of only O_2 and N_2)), while in the anode it may be binary or multicomponent, depending on the fuel mixture (for humidified H_2, the mixture is $H_2 + H_2O$; for hydrocarbons, it is $C_xH_y + H_2 + H_2O + CO + CO_2$) [30]. For this specific study only the simplest form of C_xH_y, i.e., CH_4 is included. Depending on the cell materials and operating conditions, different mass transfer models are applicable. As a consequence, there is a wide range of models to describe the mass transfer in an SOFC where in some models all three mechanisms are considered while others neglect the convective

mass flow in the electrodes. Commonly used molecular mass diffusion equations include Fick's equation for binary component diffusion or the Stefan-Maxwell equation for multicomponent ordinary diffusion for the channels and electrodes. However, Fick's equation is often not sufficient for modeling the mass transfer in SOFC as more than two components are included in the fuel. The Dusty Gas Model is sometimes used to model the mass transfer in the electrodes because its higher accuracy to a cost of increased complexity and computational power [30]. The Stefan-Maxwell model for diffusion is the most general approach for describing multicomponent mass transport. In contrast to Fick's model for the binary diffusion, it can reproduce diffusive effects of ternary mixtures, such as counter diffusion. But in the limit of binary mixtures the Stefan-Maxwell equation will reduce to Fick's equation The Stefan-Maxwell equation is often modified for the porous media by including Knudsen diffusion effects and moreover, the equation can be formulated to take into account the effect of external body forces, as well as to consider the effect of non-equilibrium behavior of the fluid [30]. Tseronis *et al.* [7] compared in 1D and 2D, the Dusty Gas model and the Stefan-Maxwell model, and found that at high hydrogen utilization and high current densities the Dusty Gas model was the most accurate in terms of validation against experimental results by Yakabe *et al.* [31] in both 1D and 2D. As the average current density increased, the differences between the 2D Dusty Gas model and the other models became more prominent.

The Knudsen diffusion coefficient of the component *i* with the component *j* in a gas mixture, $D_{k,ij}$, is calculated based on the free molecule flow theory, as described in [32]:

$$D_{k,ij} = \frac{2}{3} \cdot r \cdot \sqrt{\frac{8 \cdot \mathrm{R} \cdot T}{\pi \cdot M_{ij}}} \tag{25}$$

where r is the effective radius of the pores. The temperature dependent molecular binary diffusion coefficients (D_{ij}) are calculated by the expressions in [33], based on bi-component coefficients of the gases. The effective diffusion coefficients (eqn (26)) consider both the Knudsen and the molecular diffusion coefficients [34]. In the porous media, there is an increased diffusion length due to the tortuous paths of connected real pores and the coefficients are usually corrected by tortuosity factor (τ) and porosity (ε) [18, 32, 35].

$$D_{eff,ij} = \frac{\varepsilon}{\tau} \cdot \left(\frac{D_{i,j} \cdot D_{k,ij}}{D_{i,j} + D_{k,ij}} \right) \tag{26}$$

Equation (27) is used to describe the gas-phase species transport phenomena for each component inside the cell [28] and solved for the fuel and air channels as well as for the electrodes simultaneously, i.e., no interface condition need to be defined.

$$\nabla \left(-\rho \cdot w_i \sum^{n} D_{eff,ij} \cdot \nabla x_j + \left(x_j - w_j \right) \frac{\nabla p}{p} \bullet \vec{\mathrm{u}} \right) + \rho \cdot \vec{\mathrm{u}} \cdot \nabla w_j = S_i \tag{27}$$

where T is the temperature, x the mole fraction, w the mass fraction and S_i the (mass) source term due to electrochemical reactions.

Kanno *et al*. [36] used LBM to calculate the tortuosity factors and values between 6 and 14 are found for YSZ, between 7 and 17 for Ni as well as between 2 and 2.4 for gas-phase pore transport, respectively. Iwai *et al.* used the random walk process of nonsorbing particles as well as the LBM method to evaluate the tortuosity factors and values between 6.91 and 29.46 were found for Ni, between 9.84 and 27.89 for YSZ as well as between 1.78 and 2.06 for gas-

phase pore transport, respectively. The variations are explained by the direction (x, y and z) and by different evaluation methods [37]. Tortuosity factors in the range of 9.24 and 38.9 for Ni, and between 3.20 and 4.41 for YSZ, respectively was calculated by Vivet *et al.* [38]. Aguiar *et al.* [39] uses a gas-phase pore tortuosity factor of 6 and Bessler *et al.* [21] uses a gas-phase pore tortuosity factor of 3.5, in their respectively models. For this work the parameters for the electrode structure stated in Table 2 are employed.

Table 2: Cell parameters

Flow arrangement	co-flow
Ion conducting volume fraction	0.42
Electron conducting volume fraction	0.28
Porosity	0.30
Ion conducting support layer tortuosity factor	5
Ion conducting active layer tortuosity factor	10
Electron conducting support layer tortuosity factor	5
Electron conducting active layer tortuosity factor	10
Gas-phase tortuosity factor support layers	1.88
Gas-phase tortuosity factor active layers	3
Cell voltage	0.7 V
Average pore radius support layers	1 μm
Average pore radius active layers	0.34 μm

2.4 Heat Transport

Small SOFC systems require externally supplied heat to maintain the stack at its operating temperature, while heat removal is a challenge for larger stacks. Hot-spots can form if heat is not removed effectively, which increase agglomeration, thermal stresses and degradation in the cell components. Operating a cell below its optimal temperature significantly reduces the current generation [40]. A local temperature equilibrium (LTE) approach is applied, i.e., the temperature is assumed to be locally the same for the solid- and gas-phases (within the electrodes). The overall governing equation for the heat transport (eqn (28)) reduces to pure

heat conduction in the electrolyte layer and in the interconnectors.

$$\rho_g \cdot c_{p,g} \cdot \vec{u} \cdot \nabla T = \nabla \bullet \left(k_{eff} \nabla T \right) + Q_h \tag{28}$$

Here Q_h is the heat generation or consumption, k_{eff} the effective thermal conductivity and c_p the gas-phase specific heat. The Q_h is based on heat generation by the electrochemical reactions and on the losses through the activation, and the ohmic polarizations [23].

$$Q_h = i \cdot \left(\frac{T \cdot \Delta S_r}{n_e \cdot \mathrm{F}} + \eta_{act} \right) + \sum \frac{i^2}{\sigma} + \sum \left(r_{ref} \cdot \Delta H_{ref} \right) \tag{29}$$

where ΔS_r is entropy change of the reaction, r_{ref} is the refroming reaction rates (in mol/m^{3}s) and ΔH_{ref} the enthalpy change of the reforming reactions.

2.5 Reforming Reactions

The heat, which is generated within the cell (from the electrochemical reactions), can be used for the internal steam reforming reaction within the anode and/or outside the cell for external reforming and pre-heating of the fuel and air. The reaction kinetics from Klein *et al.* [41] for the MSR (an Arrhenius form expression dependent on the AV) is presented in eqn (30) and used to calculate the reaction rates in this work.

$$r_{MSR} = AV_{MSR} \cdot \left(943 \cdot \exp\left(\frac{-225 \cdot 10^3}{R \cdot T} \right) \cdot p_{CH_4} p_{H_2O} - 7.74 \cdot 10^{-9} \cdot \exp\left(\frac{-1937}{R \cdot T} \right) \cdot p_{CO} p_{H_2}^3 \right) \tag{30}$$

Equation (30) origins from experiments performed at Research Centre Jülish, and the anode material consists of Ni−8YSZ substrate with a standard composition of 50 wt% Ni. For AV_{MSR} an average value of $10 \cdot 10^6$ m^2/m^3 is applied in this work. It should be mentioned that

there is a disagreement in the open literature concerning the MSR rate and concerning an initial significant temperature drop. For example is the reaction rate in Achenbach and Riensche [42] significantly higher than the one in Klein *et al.*. Temperature measurements at Kyushu University, on a segmented cell, indicate that the MSR also proceeds far from the inlet, i.e., agreeing with the Klein *et al.* kinetics. It should also be mentioned that no initial significant temperature drop can be found in the segmented cell measurements from Kyushu University. Equation (30) describes phenomena occurring at the macroscale, to be compared to Hecht *et al.* [43] as well as Zhu *et al.* [12] which uses reaction kinetics with 21 reversible steps for the microscale methane reforming reaction.

Based on the global scheme for the anode, the expression for the catalyzed water-gas shift reaction from Haberman and Young [44] has been selected in this study:

$$r_{WGSR} = k_{WGSR} \cdot \left(p_{H_2O} p_{CO} - \frac{p_{H_2} p_{CO_2}}{K_{WGSR}} \right) \tag{31}$$

The rate constant (k_{WGSR}) and the equilibrium constant (K_{WGSR}) are temperature dependent expressions calculated from the experimental data, as described in [44].

2.6 Boundary conditions and parameter study

The gas inlet velocities are defined by laminar flow profiles. The inlet fuel velocity is adjusted to reach fuel utilization of 80 % for the hydrogen case. The same amount of fuel, in terms of hydrogen equivalents are supplied for the two additional cases, i.e., 30 % pre-reformed natural gas (as defined by International Energy Agency (IEA)) and 50 % pre-reformed natural gas (as defined by Kyushu University). The inlet air velocity is adjusted to

limit the average temperature difference between the inlets and outlets to 100 K for each case. At the outlets the pressure (1 atm) is fixed. The fuel inlet fractions are defined in Table 3, the air inlet is defined as air, including oxygen and nitrogen, and the outlets are defined as convective fluxes. The inlet gas temperature is defined by the operating temperature (1000 K, for all cases) and the outlet is defined as a convective flux. The boundaries at the top, bottom and center of the cell walls are defined as symmetry conditions, because it is assumed that the cell is surrounded by other ones with the identical temperature distribution. The potential at the anode current collector is set to zero and the potential at the cathode current collector is set as the cell operating voltage (0.7 V). All other boundaries and interfaces are electrically insulated.

Table 3: Inlet fuel molar fractions

	Hydrogen case	30 % pre-reformed natural gas (as defined by IEA)	50 % pre-reformed natural gas (as defined by Kyushu University)
H_2	0.90	0.263	0.399
H_2O	0.10	0.493	0.370
CH_4	-	0.171	0.115
CO	-	0.0294	0.027
CO_2	-	0.0436	0.089

3. Experimental (Kyushu University)

3.1 Fabrication of an anode-supported microtubular SOFC having segmented cathodes.

The anode Ni-8YSZ (8 mol% yittria stabilized zirconia) microtubular porous substrate (65/35 wt%, 37% porosity, Kikusui Chemical Industries Co. Ltd.) was used as the anode substrate. It had an inner diameter of 7 mm, a wall thickness of 0.5 mm and a length of 48 mm. This anode substrate was coated with 8YSZ (TZ-8YS, Tosoh Corp.) electrolyte slurry by dip-coating, being followed by co-firing at 1420 °C for two hours. Composite cathode slurry of

$La_{0.7}Sr_{0.3}MnO_3$ (LSM, Daiichi Kigenso Kagaku Co. Ltd.) and 8YSZ (TZ-8YS, Tosoh Corp.) (LSM/YSZ=10/3 wt%) was applied on the electrolyte layer by cotton swabs. Then it was fired at 1150 °C for two hours. Uniform thickness of each layer was confirmed with a scanning electron microscope after firing. We applied three cathode active areas, upstream, midstream and downstream parts along the axial direction [8]. Electrode geometrical area was 2.5 cm^2 each. Figure 3 depicts the segmented microtubular cell after firing. Silver paste was employed on the cathodes as the current collector.

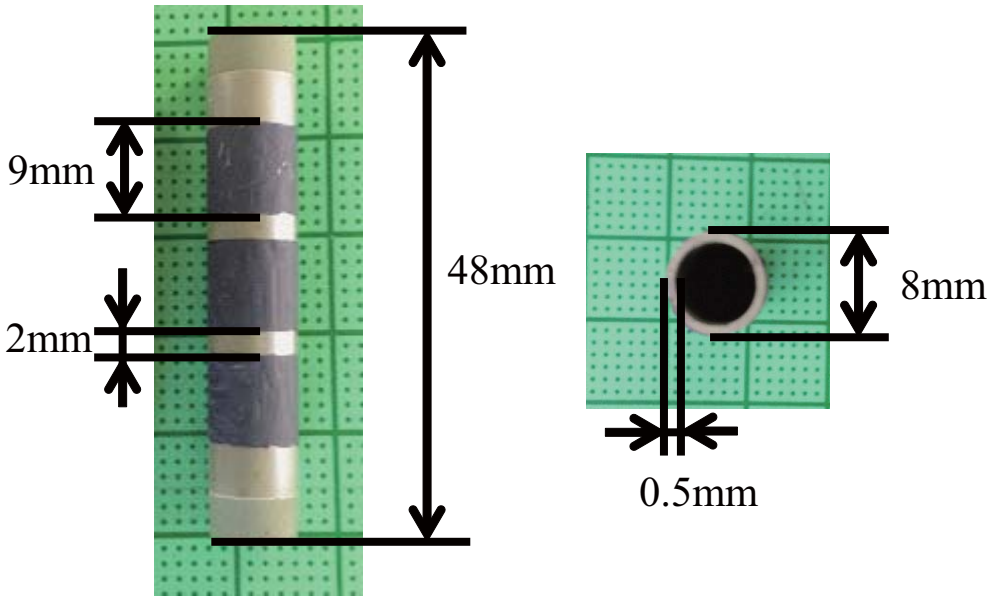

Figure 3. Anode-supported microtubular cell with the segmented cathodes.

3.2 Current and Temperature Distribution Measurements

Figure 4 illustrates the configuration of the experimental set-up. Temperature of the microtubular cell was maintained at 800 °C by an electronic furnace at open circuit voltage (OCV). The anode NiO was reduced to Ni by feeding H_2/N_2 mixture gas for two hours prior to measurements. During measurements, anode and cathode were supplied with simulated 50 % pre-reformed natural gas presented in Table 3 and air upward at 45 and 2000 cm^3min^{-1} (25 ºC), respectively, in co-flow.

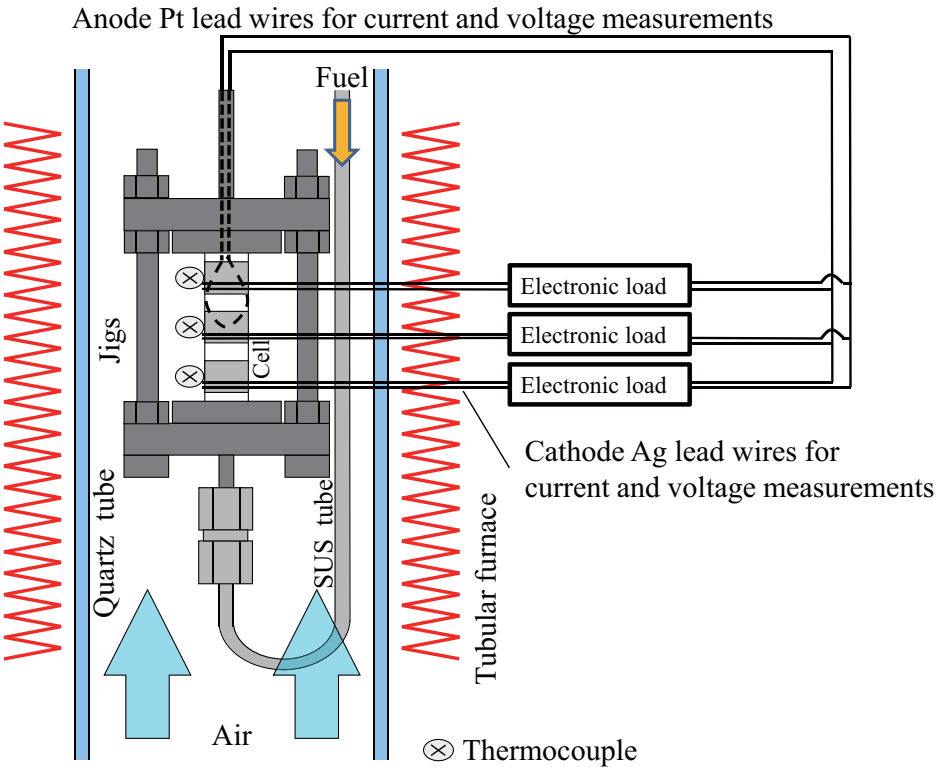

Figure 4. Experimental set-up for the characterization of the anode-supported microtubular cell having the segmented cathodes.

Current voltage (I-V) and current power density (I-P) characteristics were measured by voltage control with three electronic loads (ELZ-175, Keisoku Giken Corp.) and the anode and cathode were electrically connected with the four-terminal method. Temperatures at upstream, midstream and downstream parts along the axial direction of the cathode surfaces were measured with three thermocouples attached to the surface by silver paste. Mass flow controllers (SEC-40, Horiba STEC) were controlled by LabView 8.6 (National Instruments Inc.) on a personal computer through an I/O device (NI USB-6008, National Instruments Inc.).

3.3 Differences between the modeling cell design and the experiments

It should be noted that the model investigates planar supported SOFCs, compared to the experimental work at Kyushu University, where tubular SOFCs are investigated. However, the unique segmented cell is expected to give enough information for us to select the appropriate

MSR kinetic model. The experimental data from Kyushu University are also used for some adjustment of the AVs. For future studies it is promising to construct theoretical models describing the (segmented) tubular design as well.

4 Results and discussion

The temperature distribution for the hydrogen case is shown in Fig. 5. The strongly exothermic electrochemical reactions and the heat generation by the polarizations increase the temperature along the main flow direction. The degree of temperature increase is handled with the (inlet) air flow rate, i.e., the oxygen utilization. Note that the LTE approach is applied in our model and the temperature is assumed to be the same in the gas- and solid phase throughout the porous electrodes at each specific position.

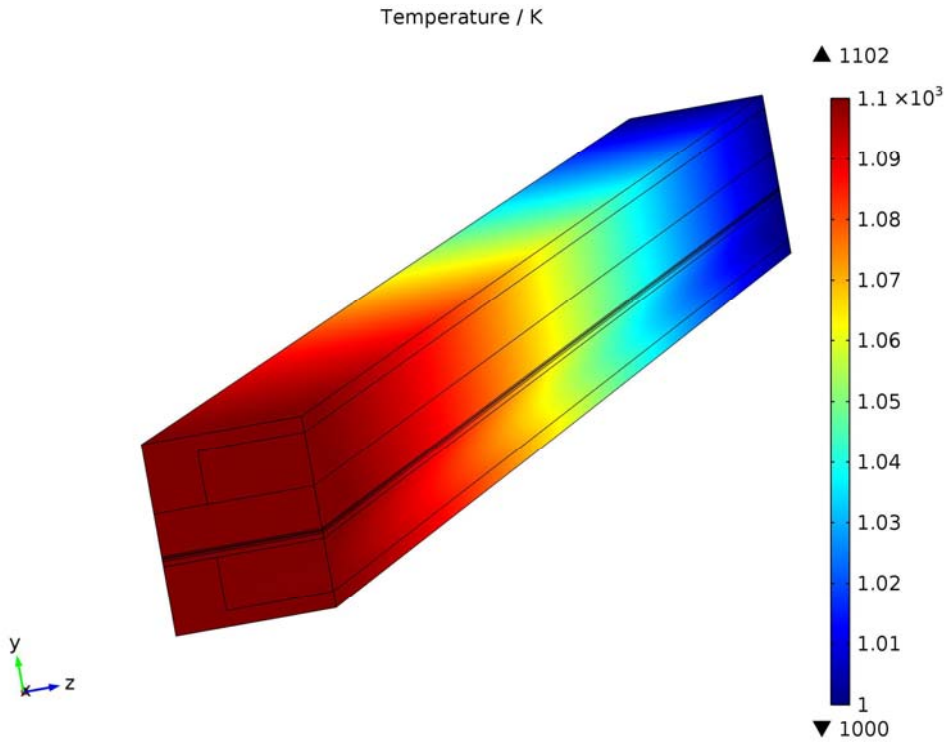

Figure 5. Temperature distribution for the hydrogen case.

Figure 6 presents the mole fraction of oxygen in the cathode side when humidified hydrogen is supplied as fuel in 3D at the cathode/electrolyte interface. Note that the color scale is identical for all figures presenting the oxygen mole fraction distribution, for easy comparison between the different cases. Oxygen is the reactant in the electrochemical reactions at the cathodic TPB. For oxygen the mole fraction gradient in the x-z-plane in the cathode (i.e., in the direction normal to the cathode/electrolyte interface) is significant, especially at positions under the interconnect ribs, due to the mass flow resistance from the relatively thin cathode (compared to the anode). Note that this effect was not possible to identify in our previous 2D models. To decrease this remarkable mole fraction gradient, the interconnect thickness between two air channels can be made thinner, the cathode support layer thickness can be increased or the cathode support layer can be manufactured with decreased gas-phase tortuosity factor compared to the ones for the cathode active layer. However, such investigations are outside the scope of this paper.

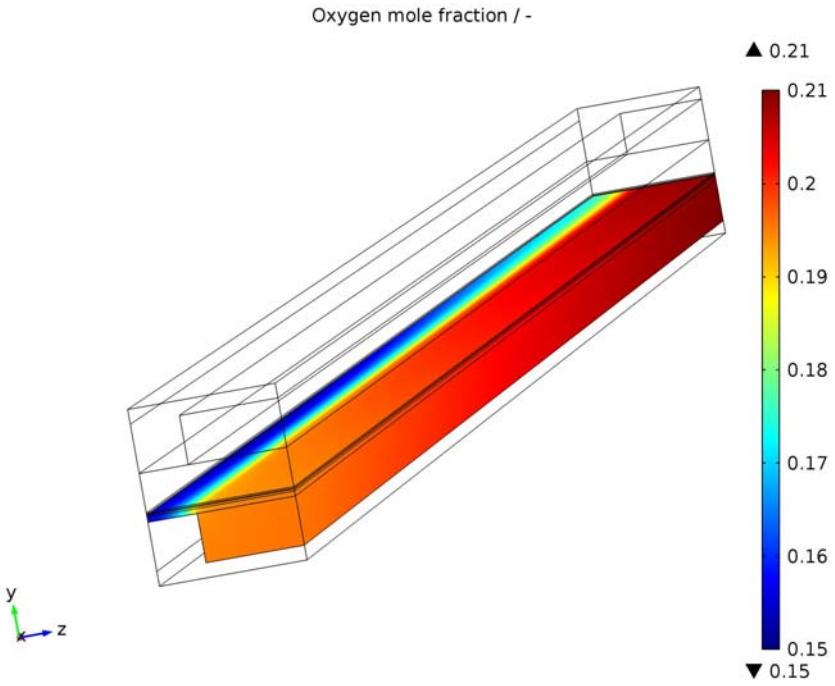

Figure 6. Oxygen mole fraction for the hydrogen case in 3D.

The electrochemical reactions at the anode TPB decrease the mole fraction of hydrogen (Fig. 7) along the main flow direction. The relatively thick anode (415 μm) enables easy transport of water from the TPB and hydrogen to the TPB, also at positions far from the fuel channel, i.e., the mole fraction gradient in the direction normal to the cathode/electrolyte interface is relatively small (compared to the case for with oxygen in Figs 6).

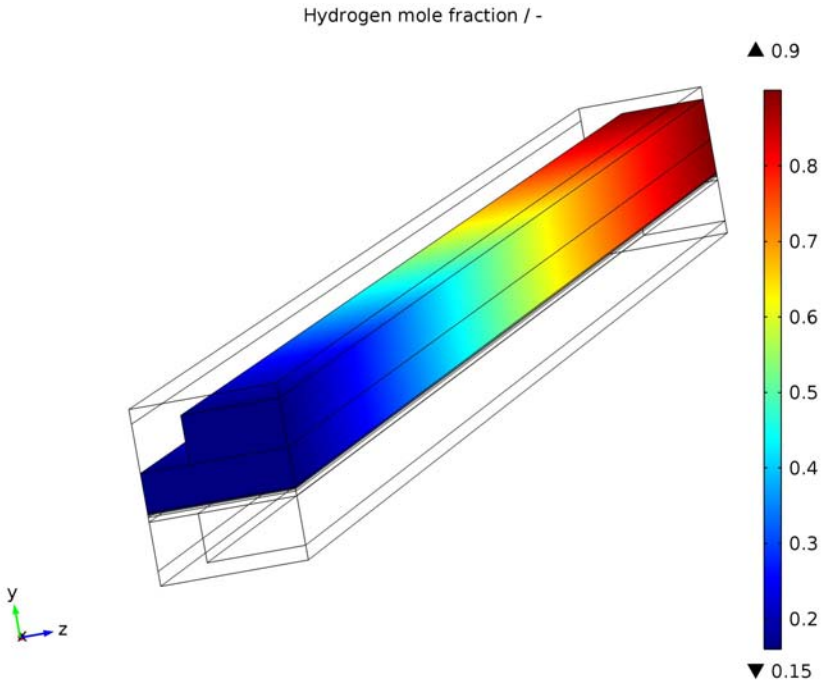

Figure 7. Hydrogen mole fraction for the hydrogen case.

The ion current density distribution at the cathode/electrolyte interface is presented in Fig. 8. The increased temperature along the main flow direction (x*-direction in Fig. 8) increases the ion current density in this direction. This increase is limited due to the production of water as well as the consumption of oxygen and hydrogen by the electrochemical reactions. In the direction normal to the cathode/electrolyte interface (z*-direction in Fig. 8) the ion current density is highest close to the channel/interconnect interfaces, i.e., where the concentration of oxygen is high and the electron transport distance is short. It should be mentioned that the scales in Fig. 8 on the axes are made dimensionless according to eqns (32)-(33).

$$x^* = x / L \tag{32}$$

$$z^* = z / W \tag{33}$$

Here, L is the cell length along the main flow direction (= 100 mm) and W is the half (due to symmetry conditions) the width of one fuel/air channel (= 1 mm) and the corresponding rib (= 0.5 mm).

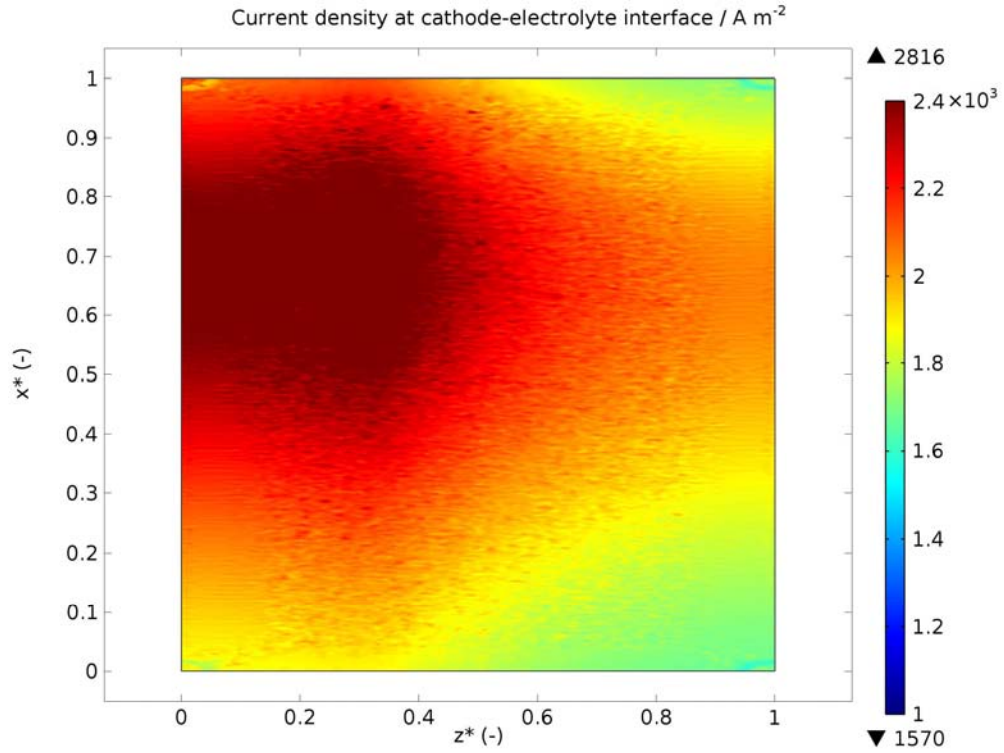

Figure 8. Ion current density distribution for the hydrogen case. (0) at the x*-axis corresponds to the inlet and (1) to the outlet. (0.333) at the z*-axis corresponds to the interconnect rib/channel interfaces. Notice that the scales on the x- and z-axes differs.

The OCV at the cathode/electrolyte interface (Fig. 9) is the highest close to the inlet, where the concentration of water and the temperature are the lowest as well as the concentrations of oxygen and hydrogen are the highest. The ongoing electrochemical reactions and the increased temperature decrease the OCV along the main flow direction (x*-direction in Fig. 9). The decrease in the OCV according to those concentrations is known as the Nernst loss

[45]. The OCV gradient in the direction normal to the cathode/electrolyte interface (z*-direction in Fig. 9) occurs due to the oxygen mole fraction gradients within the cathode in this direction.

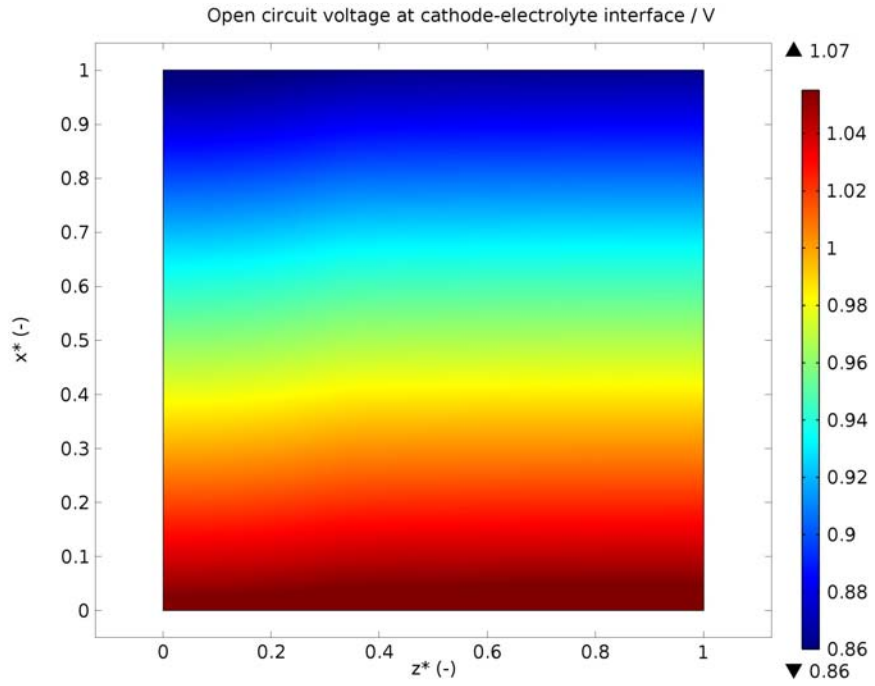

Figure 9. OCV for the hydrogen case.

The electron current density in the z-y plane at the outlet for the hydrogen case is presented in Fig. 10. It can be seen that the highest electron current density take place in the cathode at the air channel/interconnect ribs corner. A comparable behavior is found at the anode/interconnect ribs corner, but the maximum value in the anode is around 40 % of the cathode one. It can be seen that the maximum electron current density is more than ten times higher than the maximum ion current density. Notice that the electron transport in the direction normal to the cathode/electrolyte interface was not included in our previous 2D models.

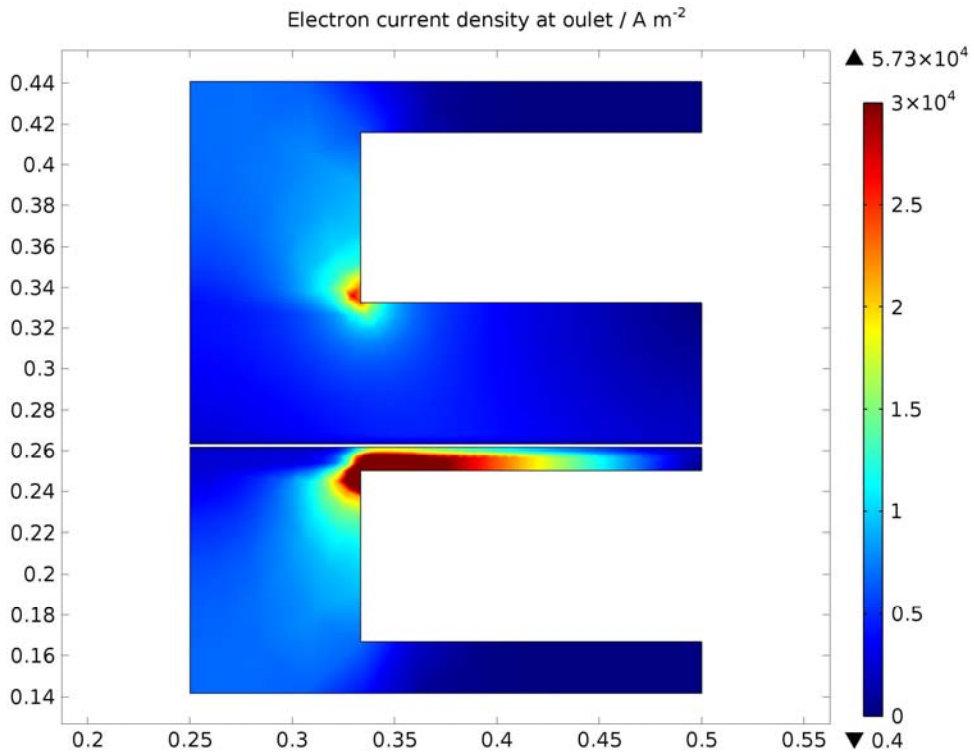

Figure 10. Electron current density at the outlet for the hydrogen case.

The oxygen mole fraction for the cases with 30 % and 50 % pre-reformed natural gas as fuel is presented in Fig. 11 and Fig. 12, respectively. The air inlet velocity is adjusted to limit the average temperature difference between the inlets and outlets to 100 K, i.e., the air utilization are significantly increased for the cases with a pre-reformed natural gas fuel mixture, compared to the case with humidified hydrogen. The decreased local fractions of hydrogen reduces the current density, which decreases the oxygen mole fraction gradient in the direction normal to the cathode/electrolyte interface, at positions under the interconnect ribs, compared to the case with humidified hydrogen (Fig. 7). Note that the case with 50 % pre-reformed natural gas as fuel has a higher current density as well as oxygen consumption throughout out the cell, compared to the case with 30 % pre-reformed natural gas. However, the air flow rate is higher for the case with 50 % pre-reformed natural, giving a decreased oxygen utilization.

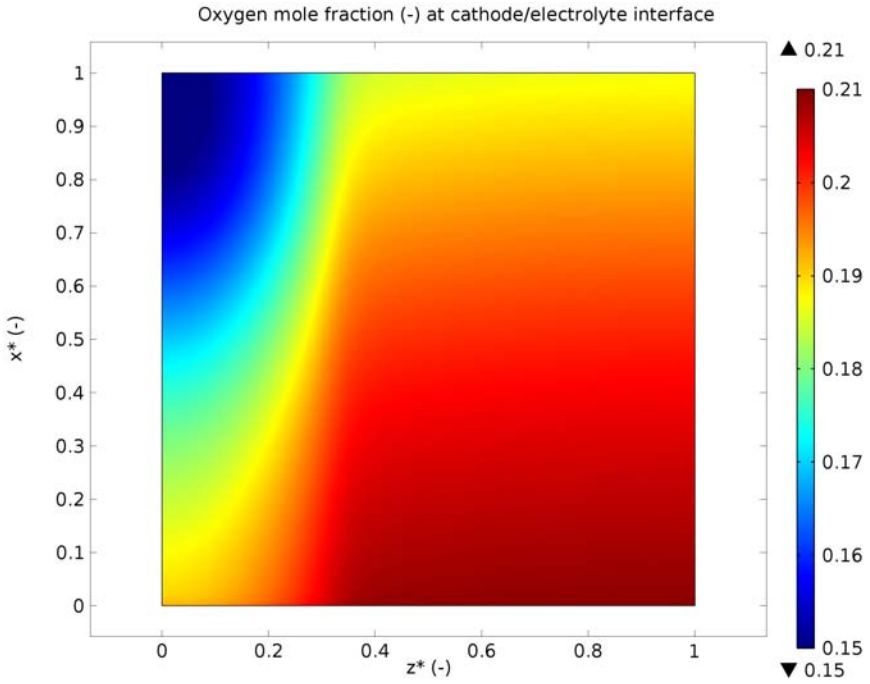

Figure 11. Oxygen mole fraction as 30 % pre-reformed natural gas is used as fuel.

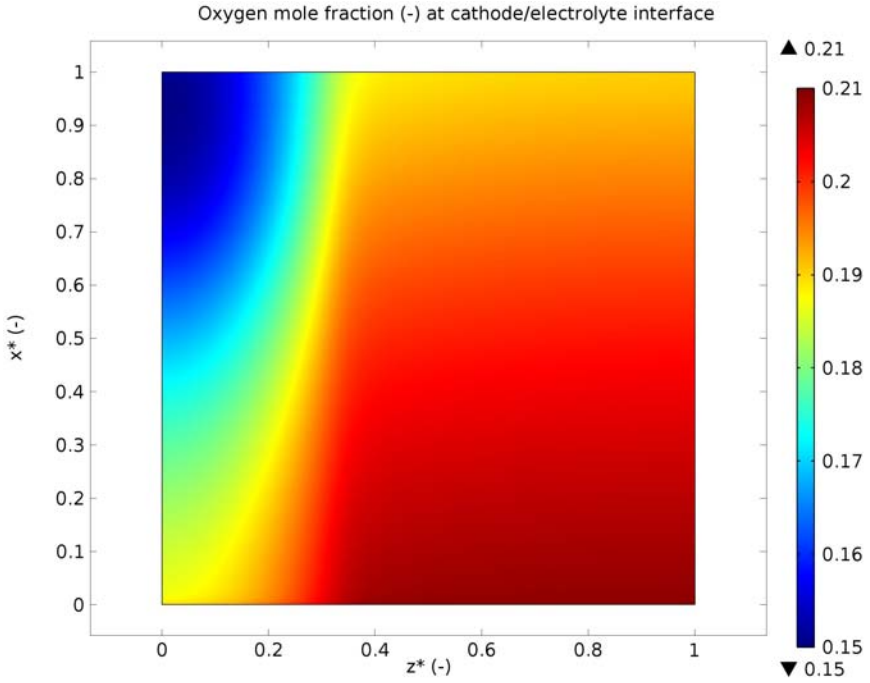

Figure 12. Oxygen mole fraction as 50 % pre-reformed natural gas is used as fuel

The hydrogen mole fraction when 30 % and 50 % pre-reformed natural gas is supplied as fuel is shown in Fig. 13 and Fig. 14, respectively. Note that the color scale is not the same for Figs 14-15, compared to Fig. 7, due to the large difference in the local mole fractions of hydrogen.

The mole fraction of hydrogen is lower when partly pre-reformed natural gas is supplied as fuel, throughout the cell, compared to humidified hydrogen, which is the main reason for the decreased OCV, which gives a decreased current density. It should me mentioned that the case with 30 % pre-reformed natural gas has a lower fraction of hydrogen at the inlet as well as throughout the cell, compared to the case with 50 % pre-reformed natural gas, which gives a higher current for the latter case.

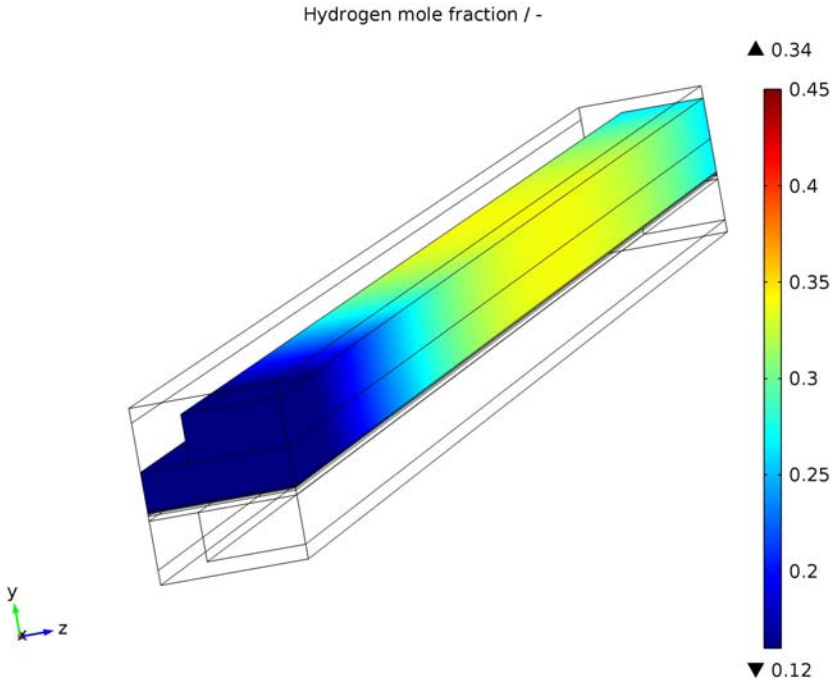

Figure 13. Hydrogen mole fraction when 30 % pre-reformed natural gas is used as fuel

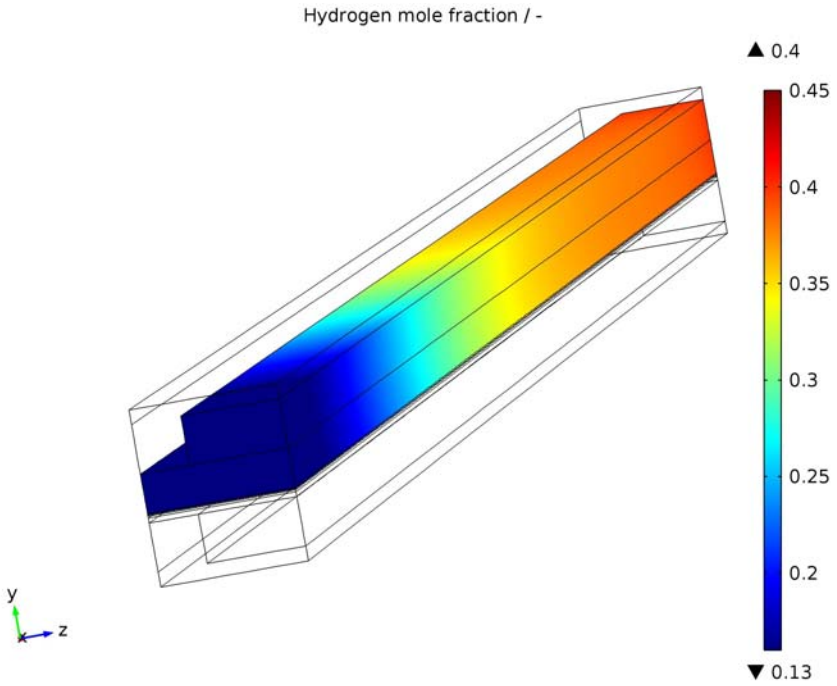

Figure 14. Hydrogen mole fraction when 50 % pre-reformed natural gas is used as fuel

The OCV behavior is similar for the cases with partly pre reformed natural gas (not shown in any figure), compared to the one with humidified hydrogen (Fig. 9). However, the maximum value (at the inlet) differs: 0.96 V for 30 % pre-reformed natural gas and 0.98 V for 50 % pre-reformed natural gas, compared to 1.07 V for the case with humidified hydrogen. On the other hand, the OCV at the outlet (also the minimum value) are 0.86 for all (three) investigated cases. Figures 15 and 16 presents the ion current density distribution at the cathode/electrolyte interface when 30 % and 50 % pre-reformed natural gas is supplied as fuel. The reduced hydrogen fraction within the anode (compared to the case with humidified hydrogen) decreases the OCV, which result in a decreased ion current density. It is also seen that the position with the maximum value is closer to the outlet when partly reformed natural gas is supplied as fuel, compared to the case with humidified hydrogen.

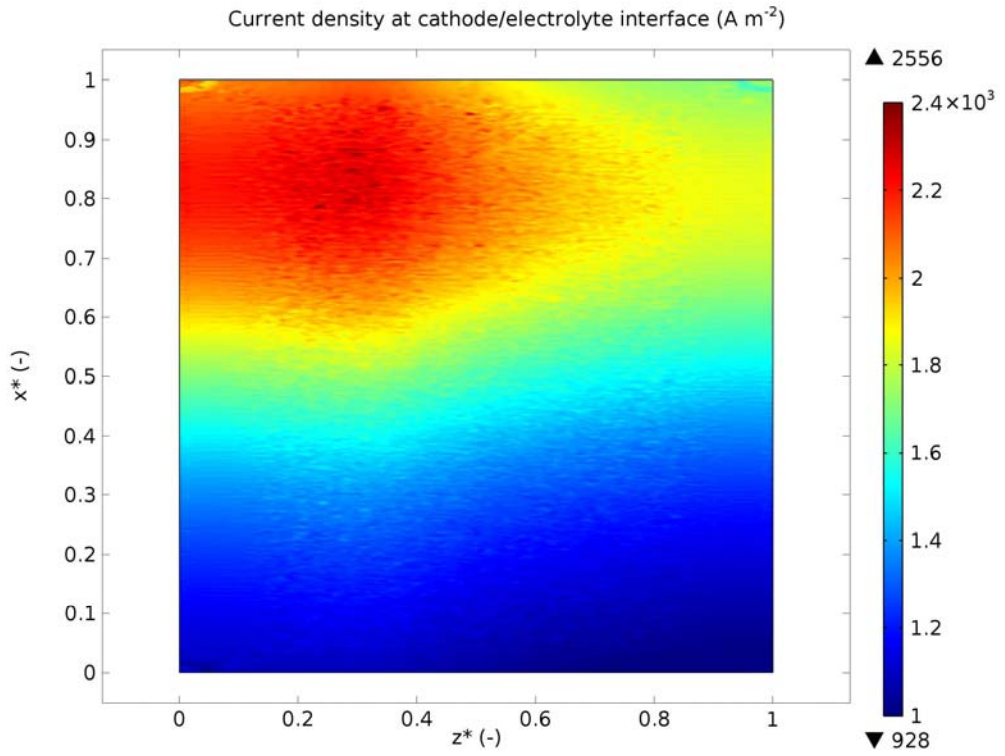

Figure 15. Ion current density distribution as 30 % pre-reformed natural gas is used as fuel

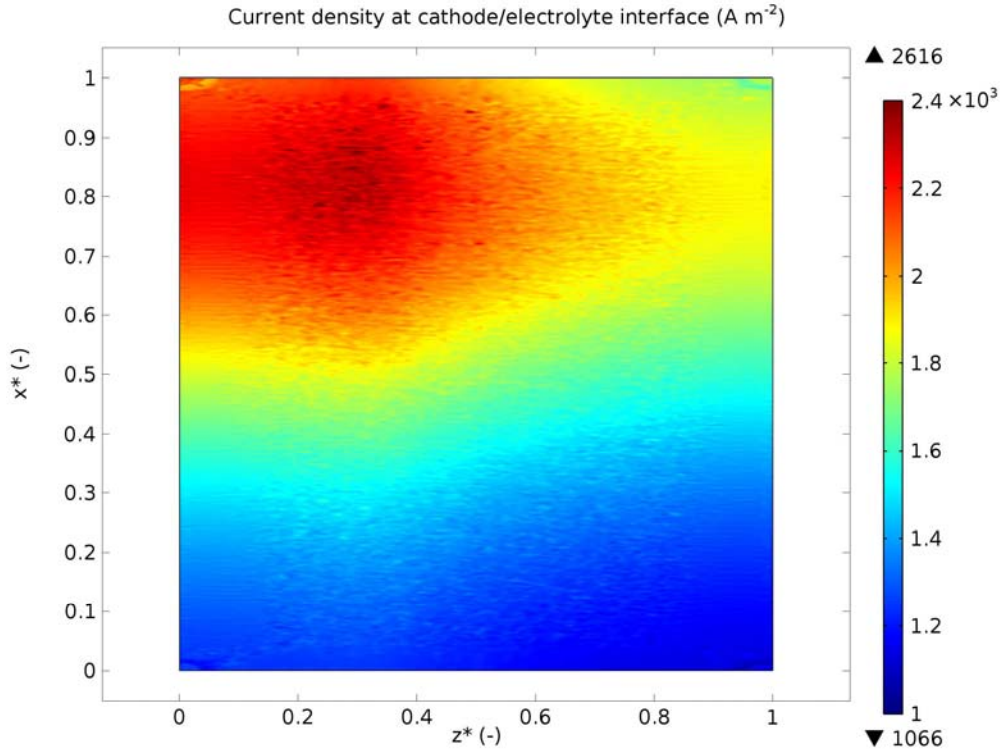

Figure 16. Ion current density distribution as 50 % pre-reformed natural gas is used as fuel

The decreased ion current density, as partly pre-reformed natural gas is supplied as fuel, decreases the requirement of electrons at the TPB, i.e., also the electron current density is decreased as is shown in Fig. 17 and Fig. 18 when 30 % and 50 % pre-reformed natural gas are supplied as fuel, respectively. It should be noted that the heat generation due to electron transport (ohmic polarization) depends on the electron current density in square, i.e., a slightly reduced electron current density can have a relatively large impact on the distribution of the different polarizations as well as on the local heat generation.

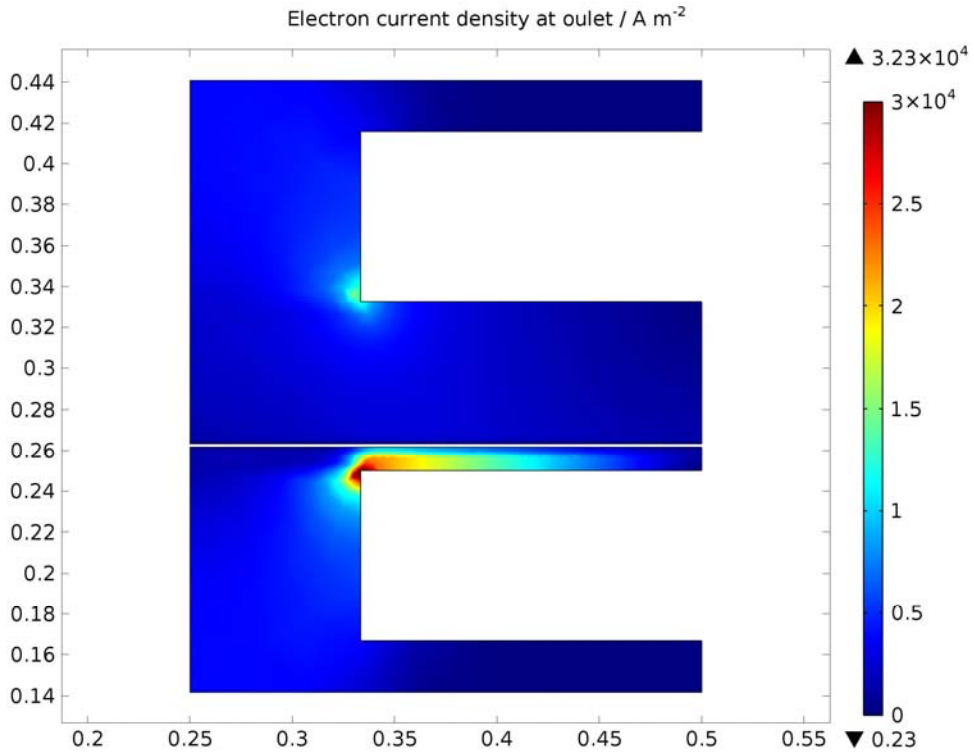

Figure 17. Electron current density at the outlet as 30 % pre-reformed natural gas is used as fuel

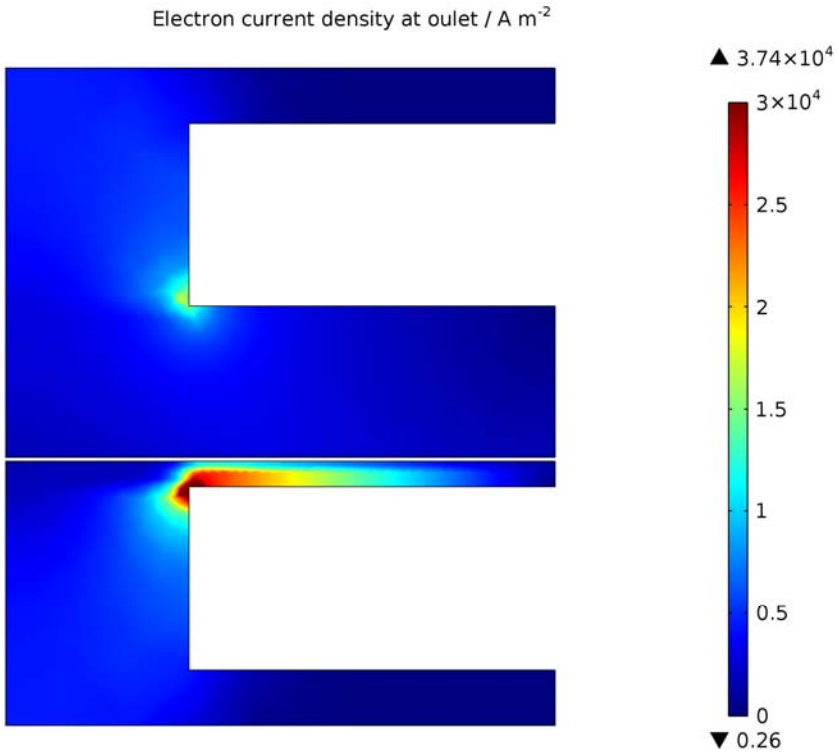

Figure 18. Electron current density at the outlet as 50 % pre-reformed natural gas is used as fuel

The MSR rate for the case with 30 % pre-reformed natural gas is presented in Fig. 19 and for the case with 50 % pre-reformed natural gas in Fig. 20. The MSR rate depends on the local temperature and the local concentrations of methane and steam, and continues to produce hydrogen and carbon monoxide as long there is still methane available. As the case with 30 % pre-reformed natural gas contains more methane (compared to the case with 50 % pre-reformed natural gas) at the inlet the reaction rate will be higher. It is found that the outlet fractions of methane are small for both investigated cases. Note that there is a significant disagreement, within the open literature, concerning the MSR rate as well as the initial significant temperature drop.

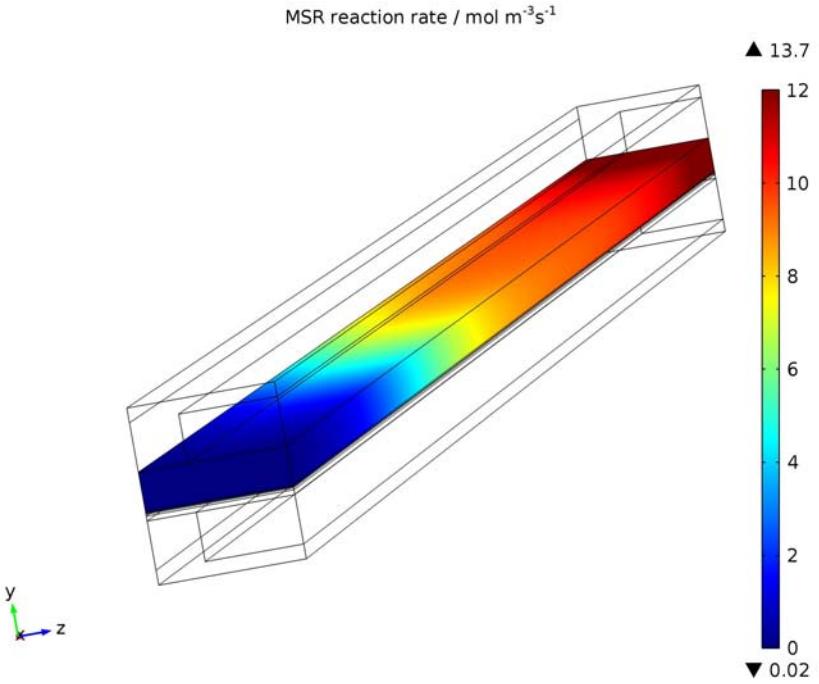

Figure 19. MSR rate as 30 % pre-reformed natural gas is used as fuel

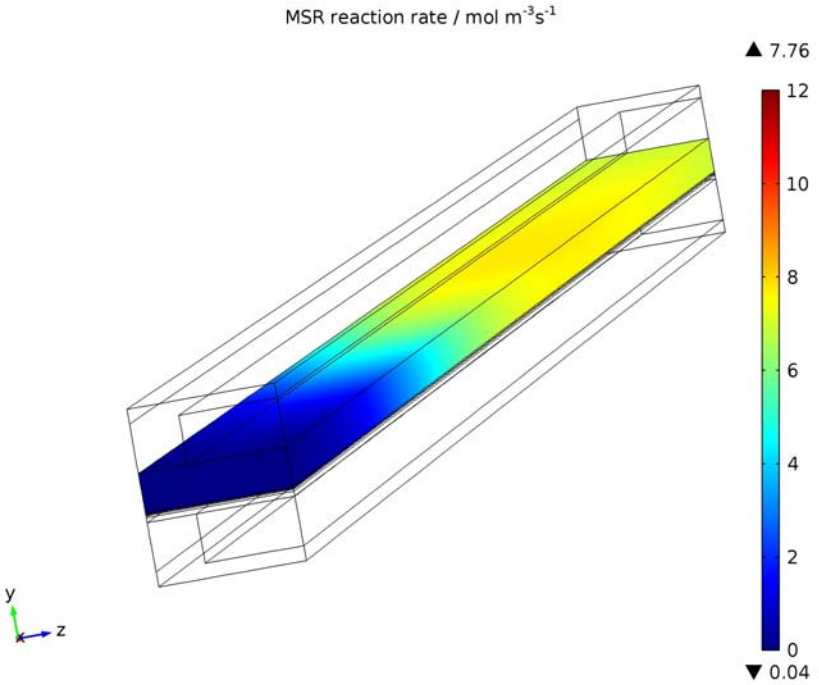

Figure 20. MSR rate as 50 % pre-reformed natural gas is used as fuel

Figures 21 and 22 shows the WGSR rate for the case with 30% and the case with 50 % pre-

reformed natural gas, respectively. It is found that the mixture with 50 % pre-reformed natural gas is relatively far equilibrium conditions, which give a high backward reaction rate at positions close to the inlet. The WGSR produces hydrogen and carbon dioxide as well as consumes carbon monoxide and steam within the anode as the electrochemical reactions proceed along the main flow direction. As a result from the internal reforming reactions, the concentration polarization is decreased and the OCV is increased, compared to the situation with no internal reforming reactions.

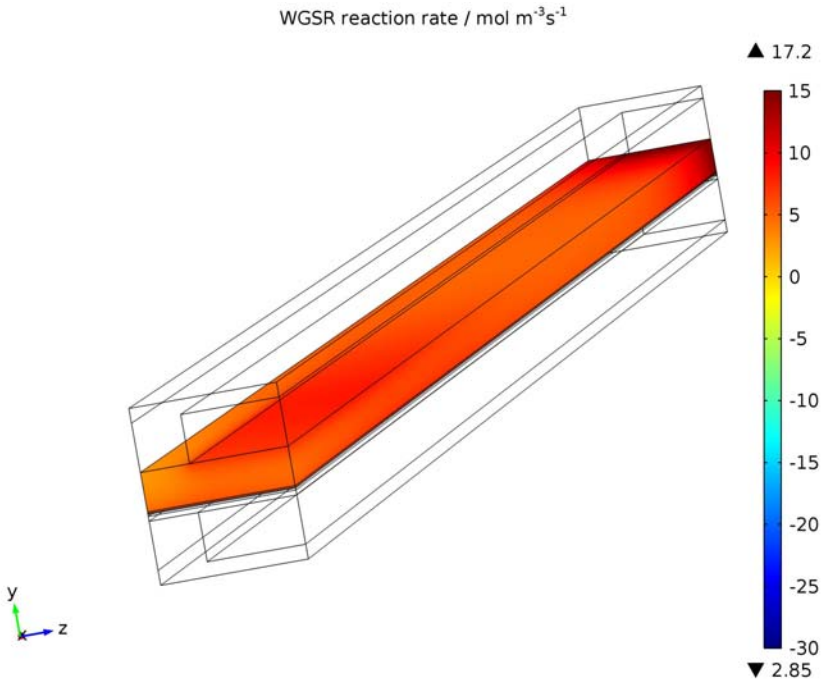

Figure 21. WGSR rate when 30 % pre-reformed natural gas is supplied as fuel

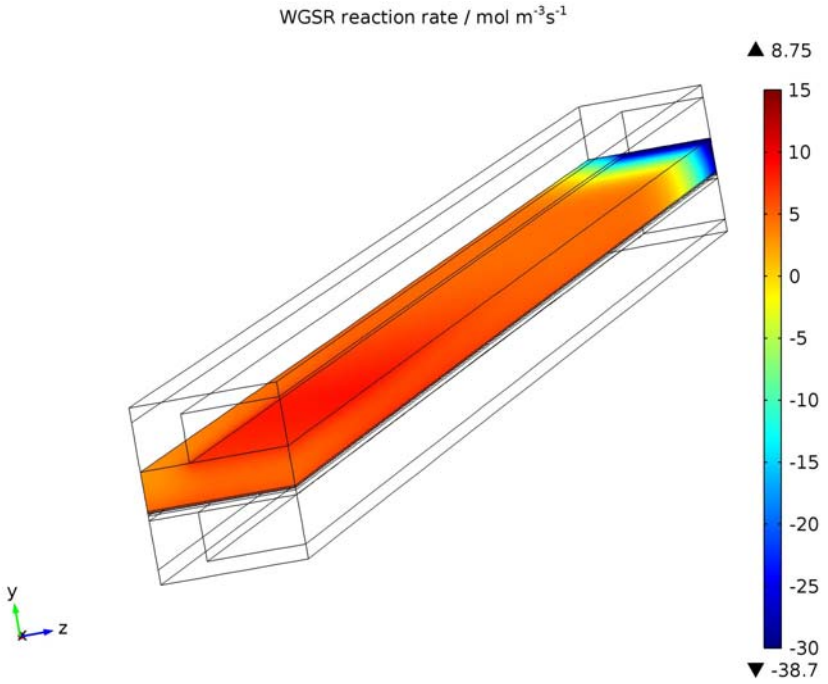

Figure 22. WGSR rate when 50 % pre-reformed natural gas is supplied as fuel

The voltage is varied (for the three cases previously presented) between 0.7 and 0.9 V and the corresponding i-v curves are presented in Fig. 23. It should be mentioned that the mass flow rates are kept constant as the voltage is varied, i.e., the air and fuel utilizations in the model are defined for a voltage of 0.7 V. Most i-v curves presented in the open literature describes experimental measurements, where significant surplus of fuel are supplied, i.e., one can not directly compare our i-v curves to the experimental ones in the open literature.

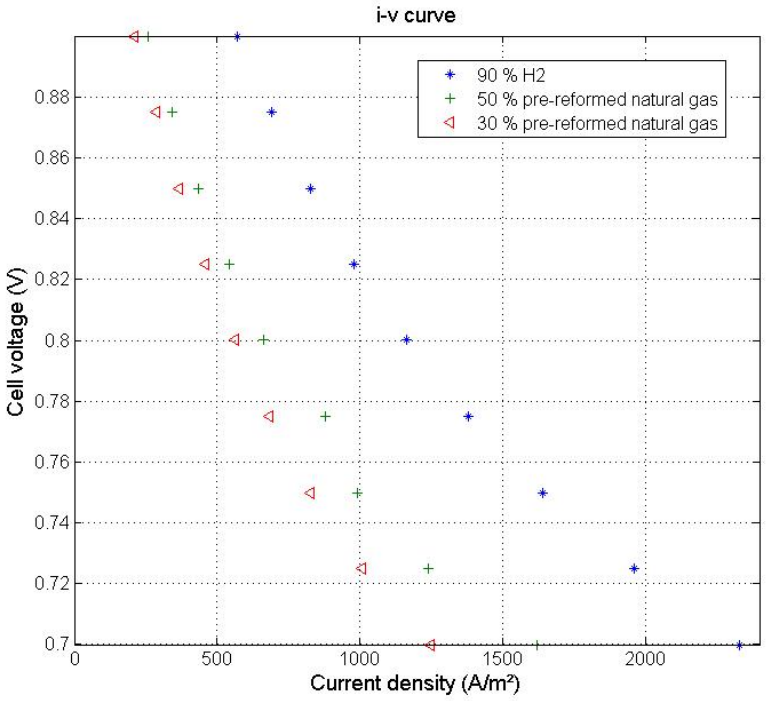

Figure 23. i-v curve for the three investigated cases

4.1 Comparison with experimental results by the microtubular cell having segmented electrodes.

Figure 24 shows the I-V characteristics for each part of the segmented microtubular cell and the sum of the currents for each segment with simulated 50 % pre-reformed natural gas presented in Table 3. In the upstream part, the OCV is lower than the other parts possibly due to slight gas leakage at microscopic crack in the electrolyte by carbon formation at the Ni particles from the cracking of dense methane near the inlet. The OCV dropped from 1.01 V to 0.80 V when the fuel was switched from H_2/N_2 mixture (40/40 cm^3min^{-1} at 25 °C) gas to the simulated reformate gas and the OCV did not recover by the H_2/N_2 mixture gas feeding again. Although this degradation often proceeds with methane rich fuel composition in general, such OCV drops cannot be observed separately without segmented electrodes.

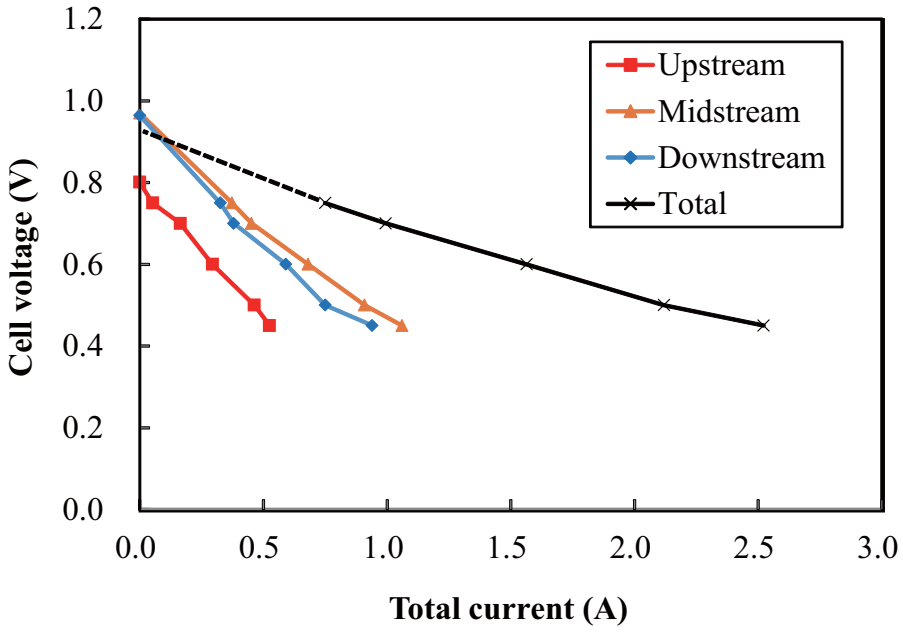

Figure 24. I-V characteristics for each part of the segmented microtubular cell

The OCVs at the midstream and downstream are 0.97 V and 0.96 V, respectively, which are in good agreement with that at the inlet in the present modeling. The currents are larger in the middle and downstream parts than the upstream at a same cell voltage. The fuel depletion in the downstream is suppressed by the smaller current in the upstream part. The current in the midstream is slightly larger than the downstream owing to smaller concentration polarization and Nernst loss with larger fuel partial pressure.

In order to confirm the MSR kinetic model, temperatures measured at each segment are compared. Figure 25 presents the surface temperatures at the segmented cathodes of the microtubular cell. The temperature difference at the OCV is not likely to come from the MSR but from the temperature distribution in the electric furnace since such difference was oberved in the case of the H_2/N_2 mixture gas as well. The temperature drop when the fuel was switched from H_2/N_2 mixture (40/40 cm^3/min) gas to the simulated reformate gas was largest in the midstream part (9°C) while it was the smallest in the upstream part (5°C), indicating

that the endothermic MSR rate is the largest in the midstream part at OCV.

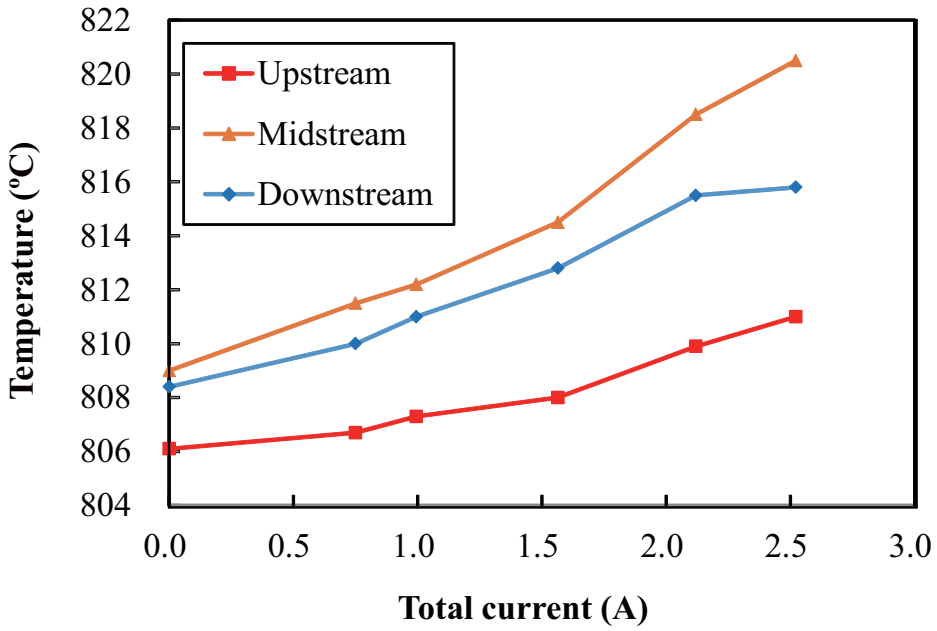

Figure 25. Surface temperatures at the segmented cathodes of the microtubular cell

The temperatures rise with the current by the heat production with the polarizations and the entropy changes, i.e. the electrochemical Peltier heats [46,47,48]. The temperature difference among the segmented electrodes under the current flow thus agrees with the current distribution in the cell shown in Fig. 24. Moreover, the difference of the temperatures among the segments are also affected by the MSR rate distribution along the fuel gas flow in the axial direction. It should be noted in Fig. 25 that the temperature rising rate becomes smaller in the high current region toward the downstream. This temperature behavior under current flow shows that the rate of the endothermic MSR becomes larger as current and toward the downstream. The consumption of H_2 and increase in the product water by the electrochemical reaction toward the downstream possibly enhance the shift of the MSR, eq. 4, to the right, resulting in the MSR rate increasing with current toward the downstream. The temperature distributions along the axial direction of the cell at OCV and under the current flow are in

accordance with the present MSR modeling that the MSR proceeds far from the inlet.

5 Conclusions

A FEM approach is applied to investigate various physical and chemical phenomena, which take place inside a single cell of a planar intermediate temperature SOFC. Equations for gas-phase species, momentum, heat, electron and ion transport are solved simultaneously and couplings with kinetic expressions for electrochemical as well as internal reforming reactions appearing in the electrodes are included.

It is found that for oxygen the mole fraction gradient in the cathode in the direction normal to the cathode/electrolyte interface is significant, especially at positions under the interconnect ribs, due to the mass flow resistance from the relatively thin cathode (compared to the anode). It is concluded that the highest electron current density take place in the cathode at the air channel/interconnect ribs corner. A similar behavior is found at the anode/interconnect ribs corner, but the maximum value in the anode is around 40 % of the cathode one. The maximum electron current density is found to be more than ten times higher than the maximum ion current density.

The fuel inlet composition is varied in a parameter study, where humidified hydrogen, 30 % pre-reformed natural gas (as defined by IEA) and 50 % pre-reformed natural gas (as defined by Kyushu University) are compared. It is concluded that when 30 % pre-reformed natural gas is supplied as fuel, the air mass flow rate is halved, compared to the case with humidified hydrogen, keeping the outlet and inlet temperatures constant. Concurrently is the fuel utilization kept at 80 %. It is concluded that the ion current density is decreased, due to a decreased OCV, because of a lower fraction of hydrogen within the anode as partly pre-

reformed natural gas is supplied as fuel, compared to the case with humidified hydrogen. Note that both the MSR and the WGSR reduces that concentration differences between the anode/fuel channel interface and the anode/electrolyte interface, which decreases the anode concentration polarization for fuel compositions containing methane and/or carbon monoxide.

The endothermic MSR rate distribution along the fuel flow in the present MSR modeling agrees with the temperature changes at OCV and under current flow measured for different segments in the segmented microtubular cell fed with simulated 50 % pre-reformed natural gas. The MSR is thereby shown to proceed far from the inlet.

6 Nomenclature

AV	active surface area-to-volume ratio [$m^2\ m^{-3}$]
c_p	specific heat at constant pressure [$J\ kg^{-1}\ K^{-1}$]
D_{ij}	molecular diffusivity [$m^2\ s^{-1}$]
$D_{ij,eff}$	average effective diffusivity [$m^2\ s^{-1}$]
$D_{k,ij}$	Knudsen diffusivity [$m^2\ s^{-1}$]
E	activation energy [$kJ\ mol^{-1}$], (actual) operating voltage [V]
E^0	open-circuit voltage at standard pressure [V]
E_{eq}	equilibrium voltage [V]
F	Faradays constant [96 485 $A\ s\ mol^{-1}$]
F	volume force vector [$N\ m^{-3}$]
ΔH	enthalpy change of reaction, [$J\ mol^{-1}$]
i	current density [$A\ m^{-2}$]
i_0	exchange current density [$A\ m^{-2}$]
k	thermal conductivity [$W\ m^{-1}\ K^{-1}$] or rate constant [-]
k_e''	pre-exponential factor [$\Omega^{-1}m^{-2}$]
K	equilibrium constant
n_e	number of electrons transferred per reaction [-]
p	pressure [atm or Pa]
Q_h	heat source term [$W\ m^{-3}$]

r	reaction rate [mol m^{-3} s^{-1}]
R	gas constant [8.3145 J mol^{-1} K^{-1}]
S_r	entropy change due to chemical reaction [J mol^{-1} K^{-1}]
S_i	mass source term [kg m^{-3} s^{-1})]
T	temperature [K]
$\vec{u}$	velocity vector [m s^{-1}]
x	mole fraction [-]
w	mass fraction [-]

Greek symbols

ε	porosity [-]
η	polarization [V]
κ	permeability [m^2]
μ	dynamic viscosity [Pa s]
ρ	density [kg/m^3]
σ	ion/electron conductivity [Ω^{-1} m^{-1}]
τ	tortuosity factor [-]
ϕ	ionic/electronic potential [V]
Ψ	viscous stress tensor, [N m^{-2}]

Abbreviations, Subscripts and Superscripts

a	anode
act	activation (polarization)
b	bulk (electrode/gas channel interface)
c	cathode
CFD	computational fluid dynamics
conc	concentration (polarization)
FEM	finite element method
i,j	species index
l	electrolyte material
MSR	methane steam reforming reaction
OCV	open-circuit voltage

ohm ohmic (polarization)

s electrode material

SOFC solid oxide fuel cell

TPB three-phase boundary

WGSR water-gas shift reaction

Chemical

CO carbon monoxide (gas phase molecule)

CO_2 carbon dioxide (gas phase molecule)

CH_4 methane (gas phase molecule)

e^- electron

LSM lanthanum strontium manganite

H_2 hydrogen (gas phase molecule)

H_2O water (gas phase molecule)

Ni nickel

O_2 oxygen (gas phase molecule)

O^{2-} oxygen ion

YSZ yttria-stabilized zirconia

7 Acknowledgments

The financial support from the Swedish Research Council (VR-621-2010-4581) and the European Research Council (ERC-226238-MMFCs) is gratefully acknowledged. The experimental work in Kyushu University was supported by Grant-in-Aid for Young Scientists (B) 23760190 from Japan Society for the Promotion of Science (JSPS).

References

[1] M. Ni, Modeling and Parametric Simulations of Solid Oxide Fuel Cells with Methane Carbon Dioxide Reforming, Energy Conversion and Management 70 (2013) 116-129.

[2] M. Ni, Modeling of SOFC Running on Partially Pre-Reformed Gas Mixture, International Journal of Hydrogen Energy 37 (2012) 1731-1745.

[3] A. Mauro, F. Arpino, N. Massarotti, Three-Dimensional Simulation of Heat and Mass

Transport Phenomena in Planar SOFCs, International Journal of Hydrogen Energy 36 (2011). 10288-10301.

[4] K. Yuan, Y. Ji, J.N. Chung, Physics-based Modeling of a Low-Temperature Solid Oxide Fuel Cell with Consideration of Microstructure and Interfacial Effects, Journal of Power Sources 194 (2009) 908-919.

[5] V.M. Janardhanan, O. Deutschmann, Numerical Study of Mass and Heat Transport in Solid-Oxide Fuel Cells Running on Humidified Methane, Chemical Engineering Science 62 (2007) 5473-5486.

[6] M. Andersson, H. Paradis, J. Yuan, B. Sundén, Three Dimensional Modeling of an Solid Oxide Fuel Cell Coupling Charge Transfer Phenomena with Transport Processes and Heat Generation, Electrochemica Acta 109 (2013) 881-893.

[7] K. Tseronis, I.K. Kookos, C. Theodoropoulos, Modeling Mass Transport in Solid Oxide Fuel Cell Anodes: a Case for a Multidimensional Dusty-Gas-Based Model, Chemical Engineering Science 63 (2008) 5626-5638.

[8] A. Shimizu, H. Nakajima, T. Kitahara, Current Distribution Measurement of a Microtubular Solid Oxide Fuel Cell, ECS Trans. 57(1) (2013) 727-732.

[9] S. Kakaç, A. Pramuanjaroenkij, X.Y. Zhou, A Review of Numerical Modeling of Solid Oxide Fuel Cells, International Journal of Hydrogen Energy 32 (2007) 761-786.

[10] K.N. Grew, A.S. Joshi, A.A. Peracchio, W.K.S. Chiu, Pore-Scale Investigation of Mass Transport and Electrochemistry in a Solid Oxide Fuel Cell Anode, Journal of Power Sources 195 (2010) 2331-2345.

[11] W.Y. Lee, D. Wee, A.F. Ghoniem, An Improved One-Dimensional Membrane-Electrode Assembly Model to Predict the Performance of Solid Oxide Fuel Cell including the Limiting Current Density, Journal of Power Sources 186 (2009) 417-427.

[12] H. Zhu, R.J. Kee, V.M. Janardhanan, O. Deutschmann, D.G. Goodwin, Modeling Elementary Heterogeneous Chemistry and Electrochemistry in Solid-Oxide Fuel Cells, J. Electrochem. Soc. 152 (2005) A2427-A2440.

[13] L. Petruzzi, S. Cocchi, F. Fineschi, A global thermo-electrochemical model for SOFC systems design and engineering, J. Power Sources 118 (2003) 96-107.

[14] H. Miao, W.G. Wang, T.S. Li, T. Chen, S.S. Sun, C. Xu, Effects of Coal Syngas Major Compositions on Ni/YSZ Anode-Supported Solid Oxide Fuel Cells, *J. Power Sources* 195 (2010) 2230-2235.

[15] T.S Li, C. Xu, T. Chen, H. Miao, W.G. Wang, Chlorine Contaminants Poisoning of

Solid Oxide Fuel Cells, J. Solid State Electrochem. 15 (2011) 1077-1085.

[16] Y. Patcharavorachot, A. Arpornwichanop, A. Chuachuebsuk, Electrochemical Study of a Planar Solid Oxide Fuel Cell: Role of Support Structures, Journal of Power Sources 177 (2008) 254-261.

[17] K. Oulmi, B. Zitouni, H.B. Moussa, H. Abdenebi, G.M. Andreadis, Total Polarization Effect on the Location of Maximum Temperature Value in Planar SOFC, International Journal of Hydrogen Energy 36 (2011) 4236-4243.

[18] H. Zhu, R.J. Kee, Modeling Distributed Charge-Transfer Processes in SOFC Membrane Electrode Assemblies, J. Electrochemical Soc. 155 (2008) B715-B729.

[19] Fuel Cell Handbook (7th edition), U.S. DoE, Morgantown, West Virginia, 2004.

[20] W. Winkler, P. Nehter, Thermodynamics of Fuel Cells, Fuel Cells and Hydrogen Energy 1 (2008) 15-50.

[21] W.G. Bessler, S. Gewies, M. Vogler, A New Framework for Detailed Electro-Chemical Modeling of Solid Oxide Fuel Cells, Electrochim. Acta 53 (2007) 1782-1800.

[22] H. Nakajima, T. Kitahara, T. Konomi, Electrochemical Impedance Spectroscopy Analysis of an Anode-Supported Microtubular Solid Oxide Fuel Cell, J. Electrochem. Soc. 157 (2010) B1686-B1692.

[23] M. Andersson, H. Paradis, J. Yuan, B. Sundén, Modeling Analysis of Different Renewable Fuels in an Anode Supported SOFC, Journal of Fuel Cell Science and Technology 8 (2011) 031013.

[24] S.B. Beale, Numerical Models for Planar Solid Oxide Fuel Cells, Transport Phenomena in Fuel Cells, Sundén B. and Faghri M. (eds.), WIT Press, pp. 42-82, 2005.

[25] M. Andersson, J. Yuan, B. Sundén, SOFC Modeling Considering Electrochemical Reactions at the Three Phase Boundaries, International Journal of Heat Mass Transfer 55 (2012) 773-788.

[26] M. Andersson, J. Yuan, B. Sundén, SOFC Modeling Considering Hydrogen and Carbon Monoxide as Electrochemical Reactants, Journal of Power Sources 232 (2013) 42-54.

[27] M. le Bars, M.G. Worster, Interfacial Conditions Between a Pure Fluid and a Porous Medium, Implications for Binary Alloy Solidification, Journal of Fluid Mechanics 550 (2006) 149-173.

[28] COMSOL Multiphysics version 4.3 User Guide, Stockholm, Sweden, 2012.

[29] M.M. Hussain, X. Li, I. Dincer, Mathematical Modeling of Transport Phenomena in Porous SOFC Anodes, International Journal of Thermal Sciences 46 (2007) 48-56.

[30] V. Novaresio, M. García-Camprubí, S. Izquierdo, P. Asinari, N. Fueyo, An Open-Source Library for the Numerical Modeling of Mass Transfer in Solid Oxide Fuel Cells, Computer Physics Communications 183 (2012) 125-146.

[31] H. Yakabe, M. Hishinuma, M. Uratani, Y. Matsuzaki, I. Yasuda, Evaluation and Modeling of Performance of Anode-Supported Solid Oxide Fuel Cell, Journal of Power Sources 86 (2000) 423-431.

[32] J. Yuan, Y. Huang, B. Sundén, W.G. Wang, CFD Approach to Analyze Parameter Effects on Chemical-Reacting Transport Phenomena in SOFC Anodes, Heat Mass Transfer 45 (2009) 471-484.

[33] R.C. Reid, J.M. Prausnitz, B.E. Poling, The Properties of Gases & Liquids (fourth edition), McGraw-Hill Book Company, New York, USA, 1987.

[34] T.X. Ho, P. Kosinski, A.C. Hoffmann, A. Vik, Modeling of Transport, Chemical and Electrochemical Phenomena in a Cathode-Supported SOFC, Chemical Engineering Science 64 (2009) 3000-3009.

[35] D.Y. Murzin, T. Salmi, Catalytic Kinetics, Elsevier Science (2005).

[36] Kanno D., Shikazono N., Takagi N., Matsuzaki K., Kasagi N., Electochim. Acta 56 (2011) 4015-4021.

[37] H. Iwai, N. Shikazono, T. Matsui, H. Teshima, M. Kishimoto, R. Kishida, D. Hayashi, K. Matsuzaki, D. Kanno, M. Saito, H. Muroyama, K. Eguchi, N. Kasagi, H. Yoshida, J. Power Sources 195 (2010) 955-961.

[38] N. Vivet, S. Chupin, E. Estrade, T. Piquero, P.L. Pommier, D. Rochais, E. Bruneton, J. Power Sources 196 (2011) 7541-7549.

[39] P. Aguiar, C.S. Adjiman, N.P. Brandon, Anode-Supported Intermediate Temperature Direct Internal Reforming Solid Oxide Fuel Cell. I: Model-Based Steady-State Performance, J. Power Sources 138 (2004) 120-136.

[40] S. Amiri, R.E. Hayes, K. Nandakumar, P. Sarkar, Modelling Heat Transfer for a Tubular Micro-Solid Oxide Fuel Cell with Experimental Validation, Journal of Power Sources 233 (2013) 190-201.

[41] J.-M. Klein, Y. Bultel, S. Georges, M. Pons, Modeling of a SOFC Fuelled by Methane: From Direct Internal Reforming to Gradual Internal Reforming, Chem. Eng. Sci. 62 (2007) 1636-1649.

[42] E. Achenbach, E. Riensche, Methane/steam reforming kinetics for solid oxide fuel cells, J. Power Sources 52 (1994) 283-288.

[43] E.S. Hecht, G.K. Gupta, H. Zhu, A.M. Dean, R.J. Kee, L. Maier, O. Deutschmann, Methane refroming kinetics with a Ni-YSZ SOFC anode support. Applied Catalysis A: General 295 (2005) 40-51.

[44] B.A. Haberman, J.B. Young, Three-dimensional simulation of chemically reacting gas flows in the porous support structure of an integrated-planar solid oxide fuel cell, Int. J. Heat and Mass Transfer 47 (2004) 3617-3629.

[45] K. Hemmes, Fuel cells, in Modern Aspects of Electrochemistry 37, R.E. White, B.E. Conway, C.G. Vayenas, and M.E. Gamboa-Adelco, eds., Kluwer Academic/Plenum Publishers, New York (2004).

[46] K. Kanamura and Z. Takehara, Temperature and Thermal Stress Distributions in a Tubular Solid Oxide Fuel Cell, Bulletin of the Chemical Society of Japan, 66 (1993), 2797-2803.

[47] S. Kjelstrup, D. Bedeaux, Jumps in electric potential and in temperature at the electrode surfaces of the solid oxide fuel cell, Physica A: Statistical Mechanics and its Applications, 244 (1997), 213-226.

[48] H. Nakajima, Electrochemical Impedance Spectroscopy Study of the Mass Transfer in an Anode-Supported Microtubular Solid Oxide Fuel Cell, in Mass Transfer – Advanced Aspects, H. Nakajima, ed., InTech, Croatia (2011) 285.